Instability of Abyssal Currents in a Continuously Stratified Ocean with Bottom Topography

MATEUSZ K. RESZKA

Applied Mathematics Institute, Department of Mathematical and Statistical Sciences, University of Alberta, Edmonton, Alberta, Canada

GORDON E. SWATERS

Applied Mathematics Institute, Departments of Mathematical and Statistical Sciences and Earth and Atmospheric Sciences, University of Alberta, Edmonton, Alberta, Canada

BRUCE R. SUTHERLAND

Applied Mathematics Institute, Department of Mathematical and Statistical Sciences, University of Alberta, Edmonton, Alberta, Canada

ABSTRACT

A theory is developed for the baroclinic destabilization of density-driven abyssal flows over topography in a rotating environment. The dominant instability mechanism being studied is the release of available potential energy caused by gradual downhill slumping of the abyssal current. The present model assumes a two-layer configuration and allows for intersections of the interface with the bottom (i.e., true fronts), as well as continuous stratification in the ambient fluid. The linear instability problem in a channel for a current with parabolic cross section is solved, and the perturbation growth rate and most unstable wavenumber are both shown to increase with current thickness. A similar trend is evident as the stratification number is increased or the current width is decreased. The instability manifests itself in the overlying ocean as an amplifying topographic Rossby wave. Alternating positive/negative pressure anomalies in the upper layer are accompanied by a wavelike deformation of the abyssal current that is most pronounced on the downslope side. Upper-layer vortical features have a distinct vertically tapered shape and are to be interpreted as bottom-intensified eddies. Long-term evolution of the flow is elucidated in a series of simulations employing the fully nonlinear governing equations. It is found that, even though the linear instability calculation relates to a periodic current, the instability characteristics are still valid to a good approximation for the case of a source flow. The abyssal current breaks up into a series of plumes that penetrate downslope into the deeper ocean, producing strong current fluctuations not unlike those observed in Denmark Strait overflow water. Furthermore, introduction of more realistic topography into the numerical simulation leads to the development of coherent baroclinic vortex pairs whose upper-layer component is strongly cyclonic.

1. Introduction

The dynamics of deep-water masses is an integral aspect of ocean circulation on both global and regional scales. Abyssal currents transport heat, salt, and nutrients as well as other chemical and biological components over great distances. The mass transport associated with bottom waters is significant. In the North Atlantic, for example, the volume flux associated with the deep western boundary current is estimated to be approximately 17 Sv (Sv $\equiv 10^6$ m^3 s^{-1}) as compared with 60 Sv for the Gulf Stream (Dickson and Brown 1994; Mellor 1996). The thermohaline circulation of the global ocean is a contributor to natural climate variability and accounts for 10%–20% of the poleward heat flux (Trenberth and Caron 2001). It has long been recognized that the overall heat budget of the oceans should include the contribution from bottom-trapped flows (e.g., Wunsch 1984). Deep waters usually form as a result of atmospheric cooling, descend through convection, and spread along the ocean bottom as concentrated currents. However, the details of this spreading (such as exact pathways and overall transports) are still not completely clear from the available observational data (e.g., Dickson and Brown 1994; Hall et al. 1997). Since general circulation models do not yet possess the spatial resolution to adequately represent the mesoscale variability associated with abyssal currents, numerical and analytical process studies are of interest. Perhaps more importantly, theoretical modeling efforts can often pin-

Corresponding author address: Dr. Gordon E. Swaters, Department of Mathematical Sciences, University of Alberta, Edmonton, AB T6G 2E1, Canada.
E-mail: gordon.swaters@ualberta.ca

point general principles and mechanisms that dominate certain types of flows. In this paper, we present a simplified dynamical theory that describes the transition to instability and subsequent evolution of density-driven benthic currents through the baroclinic release of gravitational potential energy.

Considerable interest has been generated in the past few years by observations of deep current fluctuations and intense vortices south of the Denmark Strait overflow (henceforth DSO). Reviews of observations and modeling efforts with regard to the DSO may be found in Spall and Price (1998), Jungclaus et al. (2001), and references therein. To summarize, a vein of dense water is seen to flow south through Denmark Strait and along the western slope of the Irminger Basin. The dense fluid often appears as discrete plumes, or boluses (Cooper 1955), and exhibits a high degree of time variability with a dominant period of 2–3 days (Dickson and Brown 1994). Concurrently, strong eddies roughly 30 km in diameter are generated in the ambient ocean, which travel along isobaths at an average of 27 cm s^{-1}, with a small but detectable velocity component away from the shore (Bruce 1995). While the surface flow associated with the observed vortices is predominantly cyclonic (Bruce 1995), recent hydrographic surveys also indicate the presence of anticyclones (Krauss and Käse 1998). The numerical investigation of Jiang and Garwood (1996) showed that the descent of a dense plume over linearly sloping topography results in the formation of subplumes through baroclinic instability, with an accompanying eddy field in the ambient ocean. Employing a three-layer isopycnic model, Spall and Price (1998) proposed that the development of strong cyclones is mainly caused by vortex stretching of the intermediate outflow layer, which is drawn offshore due to the thermal wind relation, rather than an intrinsic instability of the overflow waters. The recent numerical study of Jungclaus et al. (2001) indicates that the above two mechanisms are not mutually exclusive and that the instability regime depends on the local value of the Rossby number. In their computational study of DSO dynamics, Jungclaus et al. (2001) considered a bottom-trapped flow in a periodic channel domain. After geostrophic adjustment, the current was found to deform through baroclinic instability with accompanying cyclonic and anticyclonic eddies in the overlying fluid. The authors argued that subsequent intensification of the cyclones was the result of nonlinear vorticity advection. Other relevant computational efforts include Jiang and Garwood (1995), Gawarkiewicz and Chapman (1995), and Shi et al. (2001). The effect of steep topography on offshore transport was numerically investigated by Kikuchi et al. (1999), Gawarkiewicz (2000), and Tanaka and Akitomo (2001).

The evolution of deep water is important in the local dynamics of marginal seas, estuaries, and other coastal areas (Price and Baringer 1994). Episodic intrusions of bottom water off the coast of British Columbia, Canada,

are often characterized by considerable spatial and temporal fluctuations (LeBlond et al. 1991). In particular, the dynamics of deep-water replacement in the Strait of Georgia (henceforth SOG) received a great deal of attention when it became apparent that the deep current variability is associated with the development of small, bottom-intensified vortical anomalies (Stacey et al. 1991, and references therein). Based on data from a high-resolution array of current meter moorings, it was found that the eddylike features had a typical diameter of 10 km and timescales on the order of 1 day. The mechanism that generated these structures was not clear, but baroclinic instability could not be ruled out.

Swaters (1991, henceforth S91) introduced a two-layer baroclinic theory, which explicitly allows for intersections of the interface between the abyssal current and the ambient ocean with topography, unlike traditional quasigeostrophic (QG) models. Karsten et al. (1995, henceforth KST) performed a linear instability analysis of the S91 equations about an isolated parabolic front in order to determine the role of baroclinic dynamics in the SOG. Their results showed nascent plume-like features on the downslope side of the current with reasonably short timescales; however, the dominant lengthscales were somewhat longer than observations suggest. Nonlinear simulations of parabolic fronts and isolated cold domes in the context of the S91 model have been described in Swaters (1998). A more general model that includes stratification in the upper layer was found to yield shorter lengthscales than S91 (Poulin and Swaters 1999a, henceforth PSa) and was subsequently applied to the SOG by Reszka and Swaters (2001, henceforth RS). The numerical analysis of RS demonstrated the emergence of highly localized pressure anomalies and confirmed the expectation that eddies in the ambient fluid would be bottom intensified, in good agreement with available data.

Various authors have discussed the theoretical aspects of instability associated with rotationally constrained gravity currents in a general, idealized setting. Early streamtube models (Smith 1975; Killworth 1977) assumed a steady state, and could predict some average properties of dense plumes. Frontal instabilities in periodic domains were studied analytically by Griffiths et al. (1982), Paldor and Killworth (1987), Paldor and Ghil (1990), and others. However, these investigations did not include topographic effects and therefore cannot describe the baroclinic process that we are considering. A linear stability analysis of mesoscale gravity currents in the context of shallow-water theory was recently presented in Meacham and Stephens (2001). Their results are somewhat relevant to our calculation in the sense that they consider a two-layer system of finite depth, explicitly allowing for sloping topography. However, their assumptions of a homogeneous upper layer and zero potential vorticity front mean that any direct comparison with our study should be made with caution. The time-dependent, two-layer theory of S91 focused

on the release of gravitational potential energy and strong two-way coupling between the abyssal current and overlying ocean. Although this shallow-water model was derived assuming a relatively small plume thickness and topographic gradient, Jiang and Garwood (1996) believed that the S91 mechanism captured the basic type of instability seen in their numerical simulations. Similarly, Jungclaus et al. (2001) found that the initial stage of instability observed in their computational study resembled the solutions described by KST.

A number of laboratory investigations have also helped to elucidate the instability and vortex generation processes, typically using a linearly sloping bottom and constant inflow of dense fluid. Both Whitehead et al. (1990) and Lane-Serff and Baines (1998) observed a train of baroclinic vortex pairs traveling along the slope, composed of strong cyclonic flow in the ambient fluid and domed anomalies in the dense layer. Lane-Serff and Baines (2000) extended these results to the case of a stratified upper layer. Etling et al. (2000) explored two regimes of instability. The first was dominated by topographic effects and a strong source flow, while the second was dominated by rotational effects. Although cyclonic vortices in the ambient fluid were observed in both situations, the mechanism of cyclogenesis was different in each case. This dichotomy seems to support the arguments of Jungclaus et al. (2001), which suggest that the behavior of the overflow layer is highly dependent on the Rossby number. The present investigation focuses on the latter, rotationally dominant regime, in which the dense fluid is subject to plume formation through baroclinic instability. Interestingly, Etling et al. (2000) theorize that dynamics in the DSO may lie in the overlap region between these two dynamical regimes.

In this study we employ the model of PSa, which allows for continuous stratification in the upper layer and thus, we believe, offers a more complete and accurate picture of the instability than S91 while it still describes a similar dynamical limit. The analysis of PSa considered the case of a simple wedge flow without incroppings (intersections of the interface with topography), whereas here we solve the linearized equations for a more realistic current height profile that possesses both a downslope and upslope incropping. While the primitive equation numerical studies mentioned above have been relatively successful in reproducing many aspects of unstable abyssal currents, our goal is to develop a simpler theory that elucidates the underlying dynamical relationships responsible for dominant flow characteristics.

The present paper is organized as follows. In section 2 we briefly outline the model assumptions as well as the governing equations. Section 3 presents the linear stability problem and our solution technique. In section 4 we discuss the instability characteristics and spatial structure of the solutions. Section 5 deals with numerical simulations of dense plumes flowing over linear topography and demonstrates the effect of varying certain key parameters. In the same section we examine the role of bottom topography in the development of coherent baroclinic vortices. Concluding remarks and some potential avenues for future research are given in section 6.

2. Model equations

Here we give an overview of our modeling assumptions and methodology. For a detailed derivation of the present model, the reader is referred to PSa. The model employs a two-layer configuration, in which the interface is allowed to intersect the topography and the upper layer is driven by vortex tube stretching associated with deformations of the interface, in the presence of a topographically induced background vorticity gradient. An important aspect of the theory is the scaling for the abyssal current velocity. In geostrophic equilibrium, a bottom-trapped mass of dense fluid tends to follow topographic contours, with little or no cross-slope motion. Neglecting processes such as instability, interaction with the ambient ocean and Ekman draining, its steady velocity over linearly sloping topography $s*y$ is given by

$$\mathbf{u}_{\text{Nof}} = \left(\frac{-g's*}{f_0}, 0 \right), \qquad (2.1)$$

where g' is the reduced gravity and f_0 is the local Coriolis parameter (Nof 1983). While the original derivation of the Nof velocity (2.1) referred explicitly to an isolated dome of fluid in the context of one-layer shallow-water theory, a simple force balance (see the appendix) shows that (2.1) holds for each fluid parcel individually, and thus applies equally well to a current. We therefore scale the lower-layer velocity with the alongslope component of $\mathbf{u}_{\text{Nof}}$.

Given conditions favorable to instability, such a water mass will gradually give up its gravitational potential energy as it slowly descends down the incline. This mechanism is somewhat different from potential energy release to due the flattening of isopycnals since an isolated patch of lower layer fluid can, at least conceptually, migrate into deeper water without any flattening of the interface. This process cannot be described by traditional QG theory and is frequently misrepresented in numerical models that lack the necessary spatial resolution. The governing equations introduced in PSa are more general than those in S91 in that they allow the ambient layer to be continuously stratified and can describe the vertical structure of the evolving flow fields.

A schematic of the model geometry is shown in Fig. 1. Analyses of oceanographic observations imply that bottom waters often take the form of coherent, isolated patches of fluid. As mentioned previously, it is a key feature of the present model that it permits $O(1)$ variations of the interface. We assume that the density of the upper layer (layer 1) consists of a z-dependent reference density $\rho_0(z)$ plus a density fluctuation $\rho(x, y, z, t)$ that is in
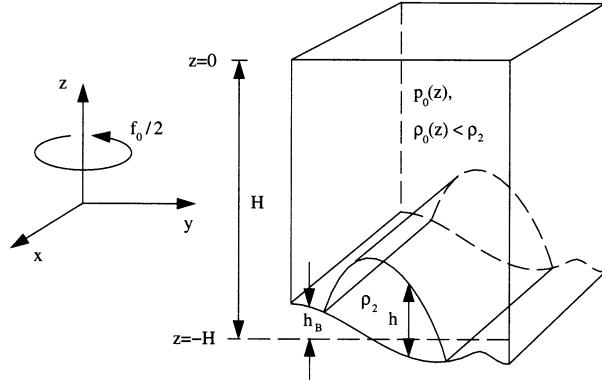
FIG. 1. Model geometry. A deep but finite continuously stratified layer overlies a thin, homogeneous layer situated on sloping, or otherwise varying, topography. The interface is allowed to intersect the topography, thus forming true fronts.

hydrostatic balance with the upper-layer dynamic pressure. The lower layer (layer 2) has a constant density, $\rho_2 > \rho_0(z)$, and its dimensional thickness scale h_* is given by δH, where H is the scale of the total fluid depth and $\delta < 1$. A scaled bottom slope parameter,

$$s = \frac{L^*}{H} s^*, \qquad (2.2)$$

is introduced where L^* and s^* are the typical length scale and topographic slope, respectively.

The relevant length scale for subinertial baroclinic processes in this regime is the upper-layer internal deformation radius,

$$L^* = \frac{\sqrt{g'H}}{f_0}, \qquad (2.3)$$

where the reduced gravity is based on the density contrast across the layer interface (to leading order, at $z = -H$); that is,

$$g' = g \frac{\Delta\rho}{\rho_2}, \qquad (2.4)$$

with $\Delta\rho = \rho_2 - \rho_0(-H)$, taking ρ_2 to be the Boussinesq reference density. The velocity scalings for layers 1 and 2 may be written, respectively,

$$U_1 = \delta\sqrt{g'H}, \qquad U_2 = s\sqrt{g'H}. \qquad (2.5)$$

The expression for U_1 results from the requirement that upper-layer velocities are principally driven by vortex stretching and compression associated with dynamic interfacial deformations. As noted earlier, lower-layer velocities are scaled according to the Nof speed. Because we want to focus on subinertial processes and filter out internal gravity wave modes, U_1 and U_2 should be small compared to the typical gravity wave speed $\sqrt{g'H}$; that is, we must have that $\delta, s \ll 1$. Surface gravity waves are filtered out by the rigid-lid approximation. We also define the ratio

$$\mu = \frac{\delta}{s}, \qquad (2.6)$$

which we formally take to be $O(1)$. The interaction parameter μ measures the influence of baroclinicity (size of δ) versus topographic effects (size of s).

Given these scalings, one can easily show that δ and s are equivalent to the Rossby numbers for the upper and lower layer, respectively:

$$\delta = \varepsilon_1 \equiv \frac{U_1}{f_0 L^*}, \qquad s = \varepsilon_2 \equiv \frac{U_2}{f_0 L^*}. \qquad (2.7)$$

By virtue of (2.7) we may interpret μ as a ratio of Rossby numbers. Again, ε_1 and ε_2 are small, and pressure in each layer is scaled so that geostrophic balance is achieved at leading order. Denoting dimensional variables by asterisked quantities, the scaling factors for the horizontal coordinates, vertical coordinate, time, upper-layer vertical velocity, and bottom topography above some reference depth are given by

$$(x^*, y^*) = L^*(x, y), \qquad z^* = Hz, \qquad t^* = \frac{L^*}{U_2}t,$$

$$w^* = \frac{U_2 h_*}{L^*} w, \qquad h_B^* = s^* L^* h_B. \qquad (2.8)$$

We note that time has been scaled advectively with the lower layer velocity, and topographic gradients, h_B^*/L^*, are small compared to the aspect ratio, H/L^*.

Introducing the scalings into the Boussinesq equations for layer 1 and the shallow-water equations for layer 2, we expand all unknown flow variables in ε_1 (or equivalently, ε_2). The resulting leading order balance on an f plane may then be written

$$[\Delta\varphi + (N^{-2}\varphi_z)_z]_t + \mu J[\varphi, \Delta\varphi + (N^{-2}\varphi_z)_z] = 0, \qquad (2.9)$$

$$\varphi_{zt} + \mu J(\varphi, \varphi_z) = 0 \quad \text{on } z = 0, \qquad (2.10)$$

$$\varphi_{zt} + \mu J(\varphi, \varphi_z)$$
$$+ N^2 J(\varphi + h, h_B) = 0 \quad \text{on } z = -1, \qquad (2.11)$$

$$h_t + J(\mu\varphi + h_B, h) = 0 \quad \text{on } z = -1, \qquad (2.12)$$

where $\varphi(x, y, z, t)$ is the upper-layer geostrophic pressure, $h(x, y, t)$ is the lower-layer thickness, $h_B(x, y)$ is the height of the topography, and $J(A, B) = A_x B_y - B_x A_y$ and subscripts refer to derivatives unless otherwise specified. The nondimensional upper-layer horizontal velocity, vertical velocity, and density fluctuation are determined from the auxiliary diagnostic relations

$$\mathbf{u}_1 = \mathbf{e}_3 \times \nabla\varphi, \qquad w = -N^{-2}[\varphi_{zt} + \mu J(\varphi, \varphi_z)],$$

$$\rho = -\varphi_z, \qquad (2.13)$$

respectively. The lower-layer velocity is given by

$$\mathbf{u}_2 = \mathbf{e}_3 \times \nabla p, \qquad (2.14)$$

where

$$p = h_B + \mu(\varphi|_{z=-1} + h) \qquad (2.15)$$

is the lower-layer geostrophic pressure. The dimensional buoyancy frequency N_* has been scaled by the natural interfacial frequency for a two-layer fluid so that the nondimensional buoyancy frequency N is defined by

$$N_* = \sqrt{\frac{g'}{H}} N, \qquad (2.16)$$

where

$$N_*^2 \equiv -\frac{g}{\rho_2} \frac{d\rho_0(z^*)}{dz^*}.$$

Equivalently, we may think of N^2 as the Burger number for the upper layer,

$$B \equiv \frac{N_*^2 H^2}{f_0^2 L^{*2}}, \qquad (2.17)$$

which is evident upon substitution of (2.3) and (2.16).

The upper-layer equation (2.9) is essentially a statement of QG potential vorticity (PV) conservation for a stratified fluid, where the parameter μ controls the size of the nonlinear terms (cf. Pedlosky 1987). The time-dependent boundary conditions (2.10) and (2.11) arise from the no-normal-flow condition at the rigid surface and at the fluid interface. The lower-layer equation (2.12) expresses conservation of mass but equivalently determines the evolution of leading order lower-layer PV, $1/h$. This model has the unsatisfying property that the leading order PV of the dense layer becomes infinite at incroppings, where h vanishes. However, it does allow description of a wide variety of frontal profiles with spatially varying PV. We do not make the assumption of a zero PV front, as has been done in some other studies (e.g., Meacham and Stephens 2001). The coupling of Eqs. (2.11) and (2.12) determines the baroclinic nature of the system as a whole. The present model is an extension of the theory presented in S91, in which both layers were assumed homogeneous. Equations (2.9)–(2.12) reduce to the S91 theory in the limit of no upper-layer stratification (see RS). Thus, in section 4, results for $N = 0$ correspond to the S91 case and, as expected, are consistent with the S91 stability analysis.

3. Linear instability analysis

We assume an x-periodic channel domain such that $-L < y < L$, and an x-invariant topography,

$$h_B = h_B(y). \qquad (3.1)$$

The lower layer is assumed to have two time-dependent incroppings, implicitly defined by

$$\zeta_i(x, y, t) = 0 \quad \text{for } i = 1, 2, \qquad (3.2)$$

where $i = 1, 2$ refers to the particular incropping. We impose boundary conditions on the upper-layer cross-channel velocity,

$$v_1 = 0 \quad \text{on } y = -L, L, \qquad (3.3)$$

and the lower-layer incroppings,

$$\left. \begin{array}{l} h = 0 \\ \dfrac{\partial}{\partial t}\zeta_i + \mathbf{u}_2 \cdot \boldsymbol{\nabla}\zeta_i = 0 \end{array} \right\} \quad \text{on } \zeta_i = 0, \quad i = 1, 2, \qquad (3.4)$$

where $v_1 = \varphi_x$ by (2.13) and $\mathbf{u}_2$ is given by (2.14), (2.15). Perturbed flow fields of the form

$$\varphi(x, y, z, t) = \varphi'(x, y, z, t),$$
$$h(x, y, t) = h_0(y) + h'(x, y, t),$$
$$\zeta_i = a_i - y + \zeta_i', \quad i = 1, 2, \qquad (3.5)$$

are introduced, where $h_0(y)$ is a known, prescribed frontal profile such that $h_0(y) > 0$ on $a_1 < y < a_2$ for constants $a_1, a_2 \in (-L, L)$. The perturbations are small, $|\varphi'|, |h'|, |\zeta_i'| \ll 1$, and in order to focus on the baroclinic aspect of the instability, there is no prescribed mean flow in the upper layer. A nonzero but depth-independent buoyancy frequency, $N = $ const, is also assumed since we would like to retain stratification while making the problem somewhat more tractable. Equations (3.1) and (3.5) are substituted into the governing equations (2.9)–(2.12) and boundary conditions (3.3), (3.4). Immediately dropping the primes, the linearized equations are given by

$$(\Delta\varphi + N^{-2}\varphi_{zz})_t = 0, \qquad (3.6)$$

$$\varphi_{zt} = 0 \quad \text{on } z = 0, \qquad (3.7)$$

$$\varphi_{zt} + N^2 h_{By}(\varphi + h)_x = 0 \quad \text{on } z = -1, \qquad (3.8)$$

$$h_t + \mu h_{0y}\varphi_x - h_{By}h_x = 0 \quad \text{on } z = -1, \qquad (3.9)$$

with linearized boundary conditions

$$\varphi_x = 0 \qquad\qquad \text{on } y = \pm L,$$

$$\left. \begin{array}{l} h + h_{0y}\zeta_i = 0 \\ \zeta_{it} - (\mu h_{0y} + h_{By})\zeta_{ix} = \mu(\varphi + h)_x \end{array} \right\} \begin{array}{l} \text{on } y = a_i, \\ z = -1, \end{array}$$

$$(3.10)$$

for $i = 1, 2$, where $h_{0y} = dh_0/dy$ and $h_{By} = dh_B/dy$.

We assume normal mode solutions for the perturbations,

$$(\varphi, h, \zeta_i) = [\tilde\varphi(y, z), \tilde h(y), \tilde\zeta_i] \exp[ik(x - ct)] + \text{c.c.} \qquad (3.11)$$

(where c.c. refers to the complex conjugate), as well as a simple, linear topography,

$$h_B(y) = \nu y \qquad (3.12)$$

for $\nu = $ const. Substitution of (3.11) and (3.12) into (3.6)–(3.10) before dropping the tildes yields a Helmholtz equation,

$$-k^2\varphi + \varphi_{yy} + N^{-2}\varphi_{zz} = 0 \qquad (3.13)$$

with the boundary conditions

$$\varphi_z = 0 \qquad\qquad \text{on } z = 0, \qquad (3.14)$$

$$\varphi_z = F(c, y)\varphi \quad \text{on } z = -1, \qquad (3.15)$$

$$\varphi = 0 \qquad\qquad \text{on } y = \pm L, \qquad (3.16)$$

where

$$F(c, y) = \nu N^2 \frac{c + \mu h_{0y} + \nu}{c(c + \nu)}. \qquad (3.17)$$

The lower-layer thickness and incroppings are now determined diagnostically by

$$h = \frac{\mu h_{0y}}{c + \nu}\varphi(y, -1),$$

$$\zeta_i = -\frac{\mu}{c + \nu}\varphi(a_i, -1), \qquad i = 1, 2. \quad (3.18)$$

Since the bottom boundary condition (3.15) involves a function of y, this system is, in general, nonseparable. This difficulty is avoided if h_0 is linear in y; that is, if the lower layer forms a wedge front without actual incroppings. In this special case F is independent of y and separation of variables may be employed. The resulting dispersion relation and corresponding solutions have been discussed in PSa and RS.

A front that is parabolic in profile is, however, more relevant for oceanographic applications. We consider fronts of the form

$$h_0(y) = \max[1 - (y/a)^2, 0], \qquad (3.19)$$

where $a > 0$ measures the half-width of the undisturbed current so that the undisturbed incroppings are located at $y = a_1 = -a$ and $y = a_2 = a$. The cross-channel gradient of the current thickness is then given by

$$h_{0y} = \begin{cases} -2y/a^2, & |y| < a \\ 0, & \text{otherwise} \end{cases} \qquad (3.20)$$

so that F retains its y dependence, making the problem nonseparable. At this point we utilize a Galerkin-type method similar to that used in Sutherland and Peltier (1994). We first expand φ in an orthonormal basis such that each of the modes individually satisfies (3.13), (3.14), and (3.16):

$$\varphi(y, z) = \frac{1}{\sqrt{L}} \sum_{m=1}^{\infty} b_m \sin Y_m \cosh\lambda_m z, \quad (3.21)$$

where

$$Y_m = \frac{m\pi(y + L)}{2L},$$

$$\lambda_m^2 = N^2 \left[k^2 + \left(\frac{m\pi}{2L}\right)^2 \right]. \qquad (3.22)$$

We note that k, $m\pi/(2L)$, and λ_m are the along-channel, cross-channel, and vertical wavenumbers, respectively. Physically, the expansion eigenfunctions represent topographic Rossby wave modes (see PSa).

Substituting the assumed solution (3.21) into (3.15), multiplying through by $\sin Y_n$, and integrating over $y \in (-L, L)$ yields the following infinite system of equations in the unknowns b_m:

$$\sum_{m=1}^{\infty} \left[\delta_{mn}(c + \nu)(c\lambda_m \sinh\lambda_m + \nu N^2 \cosh\lambda_m) - 2\frac{\mu\nu N^2}{a^2 L} \cosh\lambda_m \int_{-a}^{a} y \sin Y_m \sin Y_n \, dy \right] b_m = 0$$

$$\text{for } n = 1, 2, 3, \ldots . \qquad (3.23)$$

This linear system may be written more compactly as

$$(c^2 \mathbf{A} + c\mathbf{B} + \mathbf{D})\mathbf{b} = \mathbf{0} \qquad (3.24)$$

for appropriate coefficient matrices $\mathbf{A}$, $\mathbf{B}$, $\mathbf{D}$, where the elements of the vector $\mathbf{b}$ are the expansion coefficients b_m. Because the (unknown) complex phase speed appears quadratically in (3.24), the equation is referred to as a quadratic eigenvalue problem. Such problems arise in a wide variety of applications, including structural mechanics, acoustics, and signal processing. For an excellent survey of their applications and mathematical properties as well as relevant solution techniques, we refer the reader to Tisseur and Meerbergen (2001). Here we follow the approach of Wilkinson (1965). Since $\mathbf{A}$ is diagonal we can multiply through by $\mathbf{A}^{-1}$ and, defin-

ing the auxiliary vector $\tilde{\mathbf{b}} = c\mathbf{b}$, we obtain the doubly infinite, but otherwise standard, eigenvalue problem:

$$\begin{bmatrix} \mathbf{O} & \mathbf{I} \\ -\mathbf{A}^{-1}\mathbf{D} & -\mathbf{A}^{-1}\mathbf{B} \end{bmatrix} \begin{bmatrix} \mathbf{b} \\ \tilde{\mathbf{b}} \end{bmatrix} = c \begin{bmatrix} \mathbf{b} \\ \tilde{\mathbf{b}} \end{bmatrix}. \qquad (3.25)$$

For nontrivial solutions, c will be an eigenvalue of the system, in which case (3.25) implicitly defines a dispersion relation of the form

$$c = \hat{c}(k, \mu, \nu, N, a, L). \qquad (3.26)$$

Truncating the expansion (3.21) at a finite number of modes, M, that is, $1 \le m \le M$, allows the system (3.25) to be solved using one of several standard numerical routines. We have verified that, as the number of modes is increased, there is clear convergence to a set of dis-

tinct solutions. The results presented here were all obtained using 120 modes, which we found to be adequate for our purposes. For example, the change in maximum growth rate or the high-wavenumber cutoff was less than 1% when M was doubled to 240. Our tests, for a variety of parameter values, suggest that a truncation of $M = 120$ offers a reasonable balance between accuracy and computational cost. The system (3.25) was solved employing the routine DEIGV, provided by the U.S. Naval Surface Warfare Center.

4. Instability characteristics

a. The dispersion relation

Before we characterize the initial stages of instability with respect to various regimes of parameter space, two remarks should be made. First, we point out that the truncated eigenproblem (3.25) admits several modes of instability. The class of solutions described in this section and section 4b is that which corresponds to the highest growth rates for a given set of parameter values. This family of solutions also exhibits a single extremum in the cross-channel direction. We refer to these modes as primary modes of the instability. Secondary modes, with smaller growth rates and a more complicated cross-channel structure, are discussed in section 4c. Second, we note that in the rest of section 4 it is assumed that $L = 3.0$. We have found that the instability characteristics are not significantly affected by varing the channel width, $2L$, as long as the channel is wide enough to allow deformation of the incroppings. In the results that follow, the distance between an incropping and the closest boundary is at least as large as the current half-width. In general, however, we find that there is a tendency for length scales and timescales to increase with increasing L.

Setting $N^2 = \nu = a = 1.0$, (3.25) was solved with three different values of the interaction parameter, μ. In Fig. 2a we plot primary mode perturbation growth rates, $\sigma = kc_I$, versus along-channel wavenumber k, for $\mu = 1.0$, 2.0, and 3.0. While there is no low-wavenumber cutoff, there is a high-wavenumber cutoff in all three cases. As μ increases, so do the maximum growth rate, the value of the most unstable wavenumber, as well as the range of unstable wavenumbers. This is consistent with the analysis of S91 for parabolic coupled fronts. Physically, the trend may be interpreted as follows. Increasing μ is equivalent to increasing δ, while keeping s fixed. As the depth fraction is increased, the fluid becomes more baroclinic, leading to larger growth rates and shorter wavelengths. Similarly, if we interpret δ as the upper-layer Rossby number [see (2.7)], we see that growth rates increase when the upper-layer inertial terms become more important. As was alluded to previously, Fig. 2a demonstrates that the most unstable wavenumbers are larger in the present model, for nonzero N, than those obtained for the S91 model with the same parameter values. This trend is discussed further below. Phase

speed curves corresponding to Fig. 2a are displayed in Fig. 2b. The speeds are all negative, that is, moving in the direction of the mean flow in the present channel geometry. The curves show very little change in the unstable range of wavenumbers as μ is increased. They are however, fairly dispersive. Figure 2b also suggests that this mode of instability results from a coalescence of two Rossby wave modes.

Increasing N, the nondimensional buoyancy frequency, has a similar effect to that of increasing μ, as Fig. 3a demonstrates. Setting $\mu = 2.0$ and $\nu = a = 1.0$, we solved (3.25) for $N^2 = 0.5$, 1.0, and 1.5. Again, with increasing N, the growth rate for any given wavenumber is increased, as is the high-wavenumber cutoff. This is reasonable on physical grounds since increasing the stratification inhibits vertical motions. A density stratified fluid disturbed from below may be characterized by an effective depth (see Lane-Serff and Baines 2000), above which perturbations are damped out and isopycnal departures become negligible. This depth, where it is smaller than the actual depth, will determine the qualitative behavior of the fluid. Thus, in the present model, increasing N corresponds to decreasing the effective thickness of the upper layer, which, in essence, makes the system more baroclinic without increasing μ. As above, the increased baroclinicity is manifested in a more vigorous, localized instability. While not shown, the analogous σ curve for $N = 0$ (i.e., the S91 case) is smaller than all three curves in Fig. 3a, with a maximum of 0.7 at $k = 1.2$ (see Table 1). Figure 3b contains a plot of the phase speed curves corresponding to Fig. 3a. We can see that c_R becomes more dispersive at low wavenumbers as N is decreased.

Next, the half-width, a, of the current was varied while the other parameters were held fixed; that is, $\mu = 2.0$, $\nu = N^2 = 1.0$. Figure 4a demonstrates growth rate curves for $a = 0.5$, 1.0, and 1.5. The opposite trend from the previous two cases is apparent, in the sense that both the growth rates and range of unstable wavenumbers decrease with increasing a. Similarly, as the current width becomes smaller, the dominant wavelength of the instability increases. This result is consistent with the findings of S91. We plot the corresponding phase speed curves in Fig. 4b.

For easy reference, Table 1 contains selected quantitative results which characterize the instability, with $a = \nu = 1.0$. For the most-unstable wavenumber $\hat{k}$, we have tabulated the corresponding length scale $\hat{\lambda}$, phase speed $\hat{c}_R$, and growth rate $\sigma_{max} = \sigma(\hat{k})$. It is useful at this point to cast the same quantities in terms of dimensional variables. We choose scaling parameters applicable to the SOG, following the work of KST. Based on available data, the case $\mu = 1.0$ is the most relevant for dynamics at depth in the SOG. The other entries are provided for comparison purposes, where an increase in μ may be interpreted as a thicker lower layer and a higher value of N corresponds to a larger Burger number for the ambient ocean. Vertical density profiles in the
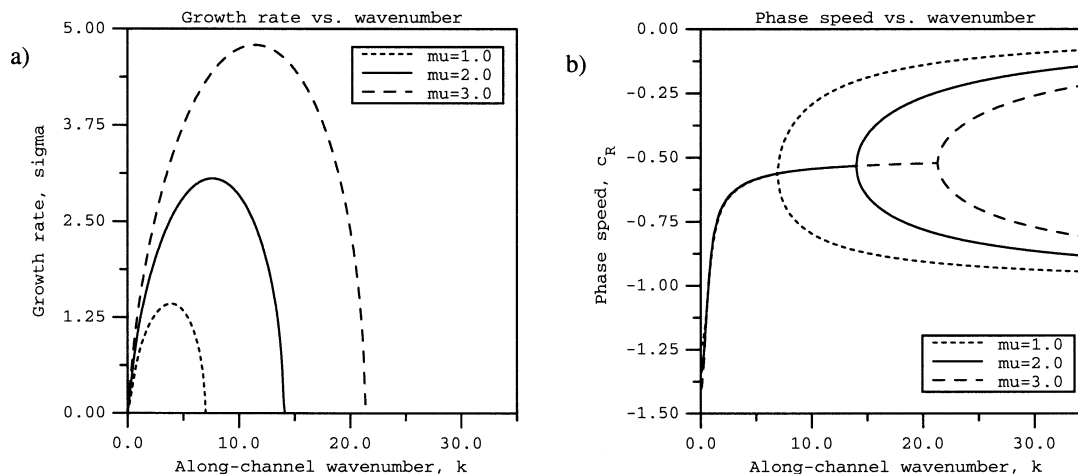
FIG. 2. (a) Growth rates $\sigma = k c_I$, and (b) phase speeds c_R vs along-channel wavenumber k, corresponding to the primary mode of instability for $\mu = 1.0$ (dotted lines), $\mu = 2.0$ (solid lines), and $\mu = 3.0$ (dashed lines). In both plots, $\nu = a = N^2 = 1.0$.

northern part of the strait suggest $0.5 < N^2 < 1.0$ as a reasonable estimate (LeBlond et al. 1991). While a linearly sloping topography is a poor approximation of the SOG bathymetry, KST utilized a piecewise-linear topography in their calculation such that the current was initially located on one linearly sloping surface. It is not unreasonable, therefore, to compare our results with those of KST in a quantitative way. In the notation of section 2, we assume that $H = 300$ m, $h_* = 65$ m, and $s^* = 9 \times 10^{-3}$. The dynamical length scale, that is, the upper-layer deformation radius, is $L^* = 7.3$ km while the timescale is about 12 h. Accordingly, Table 1 also contains the dimensional quantities λ^*, c_R^*, and T_e^*, that is, the dominant wavelength, phase speed, and e-folding time, respectively.

In the case $\mu = N^2 = 1.0$, Table 1 shows that the dominant along-channel wavelength is about 12 km and the e-folding time is several hours. This is in good agreement with the results of Stacey et al. (1991), who describe the flow field as highly dynamic with eddy diameters on the order of 10 km. The linear analysis of KST predicted length scales of about 40 km in this parameter regime. It appears that introducing upper layer stratification results in lengthscales and timescales that are in better agreement with the SOG observations. An issue that must be addressed is the relationship between the results of linear theory and subsequent nonlinear evolution. It is not immediately obvious that the dominant wavelength in the linear regime will lead to coherent, long-lived features of a similar size in the nonlinear regime. Nevertheless, the assumption is often made (e.g., Griffiths et al. 1982; KST; Meacham and Stephens 2001) and we discuss its validity in the context of S91 and PSa in section 5.

b. Perturbation spatial structure

In this section we describe the spatial structure of the primary mode of instability. Figures 5 and 6 are cross sections of the upper-layer streamfunction φ for $\mu = N^2 = \nu = a = 1.0$. The along-channel wavenumber has the value $k = 3.9$, which corresponds to the most unstable mode in this parameter regime (see Fig. 2a). Physically, if the parabolic-front current is perturbed by a small-amplitude random wavefield, the wavelength expected to dominate the flow is $2\pi/3.9 \approx 1.61$, at least until nonlinear effects become important. Using our SOG scalings, Table 1 suggests a dimensional wavelength of about 12 km. The instability manifests itself in the upper layer as high and low pressure anomalies aligned along the downslope edge of the current in an alternating pattern. The contour plots in Figs. 5a, 5b, and 6 represent upper-layer sections at $z = -1$, $z = 0$, and $y = -0.84$, respectively. We can see from Fig. 5 that the perturbation is bottom intensified (its amplitude at the surface, $z = 0$, is about 50 times smaller than at the bottom, $z = -1$). The vertical section in Fig. 6 was taken at $y = -0.84$, slightly upslope of the lower incropping, since this is where the pressure anomalies were most intense. Again, the bottom-intensified nature of upper layer flow is evident. We interpret these pressure anomalies as vertically tapered eddies, not unlike bottom-intensified vortices often associated with bottom-trapped plumes and cold domes propagating along continental shelves. It is also important to point out that the anomalies in Fig. 5 are highly localized in the cross-channel direction, which is consistent with the Stacey et al. (1991) survey. The KST solutions, on the other hand, exhibit upper-layer vortices that extend over the entire width of the channel.

In Fig. 7a we plot the perturbed total lower-layer thickness [i.e., $h_0(y) + h'(x, y, t_0)$], corresponding to the upper-layer plots in Figs. 5 and 6. The downslope front has been deformed by the wavelike perturbation. While a similar deformation of the upslope front also exists, it is much weaker and cannot be discerned from
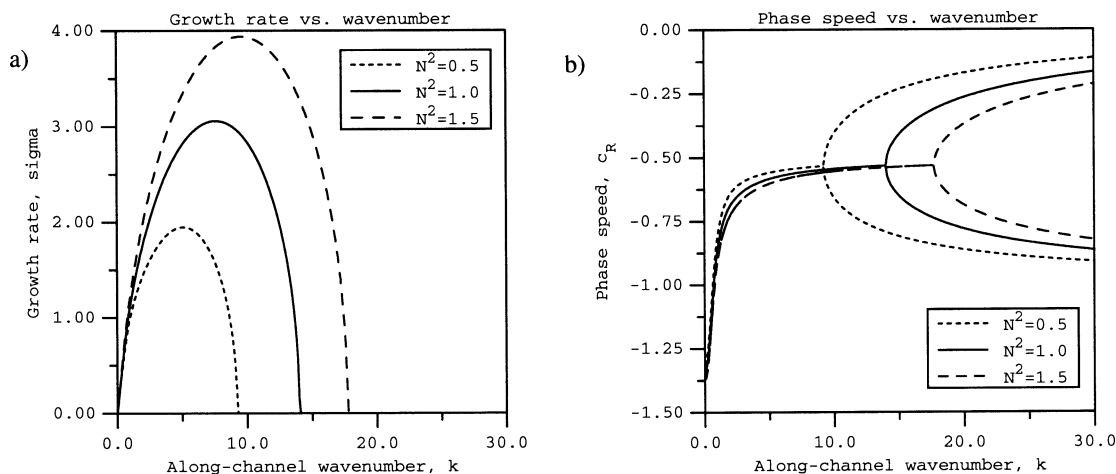
FIG. 3. Same as Fig. 2 but for $N^2 = 0.5$ (dotted lines), $N^2 = 1.0$ (solid lines), and $N^2 = 1.5$ (dashed lines). In both plots, $\mu = 2.0$, and $\nu = a = 1.0$.

the contour plots. This asymmetry is not surprising since it clearly takes energy for fluid parcels to move up the slope, while moving down the slope releases energy. As the perturbation grows, dense plumes of lower-layer fluid descend into deeper water. Qualitatively, the plumes resemble the initial stages of bottom water spreading seen in numerical simulations of Gawarkiewicz and Chapman (1995), Jiang and Garwood (1996), as well as Jungclaus et al. (2001). It must be noted that the amplifying upper-layer Rossby waves are shifted slightly upstream of the corresponding lower layer anomalies (cf. Figs. 5a and 7a). We interpret this phase difference as a vertical tilt of the unstable wave into the mean flow, which is the configuration favored by baroclinic energy release (Pedlosky 1987). A contour plot of the lower-layer geostrophic pressure (2.15) is plotted in Fig. 7b. Although the pressure, that is, the streamfunction, is defined everywhere in the domain, it is only appropriate to consider lower layer velocities in the region where the layer thickness is nonzero, as shown in Fig. 7a. The pressure is a monotonically increasing function of y, indicating that the velocity is everywhere negative.

c. Secondary modes of instability

The solutions we have discussed up to this point represent only the family of fastest-growing solutions to

(3.25). Other solutions exist, however, whose instability characteristics we now describe. As an example, for $\mu = 3.0$, $N^2 = \nu = a = 1.0$, we have found four distinct solutions, whose growth rates are plotted in Fig. 8. Growth rate curve (a) in Fig. 8 is the same primary mode as the dashed line in Fig. 2a. The secondary modes in Fig. 8 are characterized by smaller growth rates for any given unstable wavenumber k. Thus the σ curves in Fig. 8 have been given the labels (a), (b), (c), and (d) in order of decreasing maximum growth rate, σ_{max}, over all unstable k. While these secondary solutions are unlikely to be realized physically starting from an infinitesimal disturbance, they may still emerge if a perturbation with the right wavenumber is of sufficient amplitude to push the system close to the nonlinear regime. The linear analysis of S91 identified a second distinct mode of instability for parabolic fronts with smaller growth rates than the primary mode. This mode only existed beyond $\mu \approx 3.5$, whereas in the continuously stratified case the first secondary mode already appears at $\mu \approx 0.1$.

The connection with the S91 theory also becomes apparent in the perturbation spatial structure. The solutions discussed in the previous section have a single extremum in the cross-channel direction (see Fig. 5), and correspond to the "monopole" solutions in S91. The secondary mode in S91 was called a "dipole," as

TABLE 1. Dispersion characteristics for various values of μ and N^2, with $a = \nu = 1.0$. We define $\hat{k}$, $\hat{\lambda}$, and σ_{max} to be the most-unstable wavenumber, dominant wavelength, and maximum growth rate, respectively. The asterisked quantities λ^*, c_R^*, and T_e^* are the dimensional dominant wavelength, phase speed, and e-folding time, respectively. Other symbols are defined in the text.

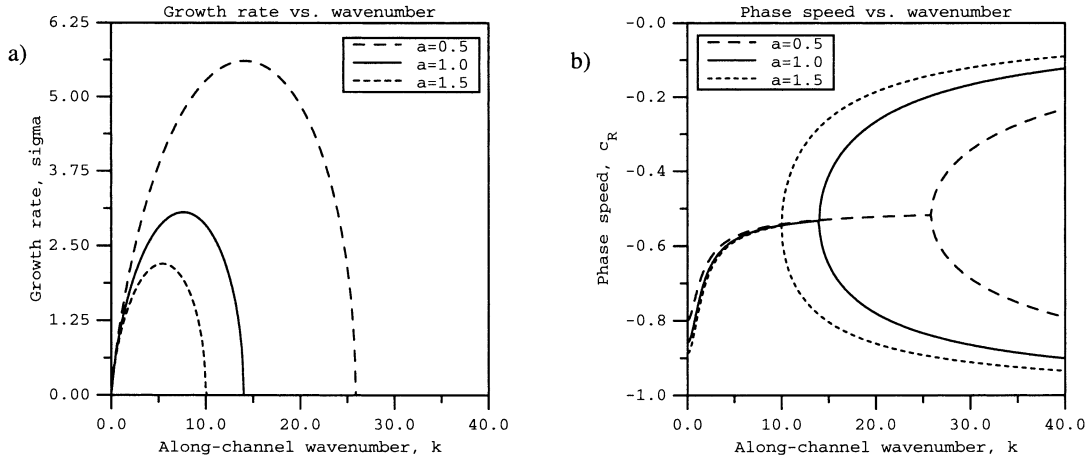| μ	N^2	$\hat{k}$	$\hat{\lambda}$	$\hat{c}_R$	σ_{max}	λ^* (km)	c_R^* (cm s^{-1})	T_e^* (h)
1.0	1.0	3.9	1.61	−0.61	1.42	11.8	−10.0	8.5
2.0	1.0	7.6	0.83	−0.56	3.06	6.0	−9.2	3.9
3.0	1.0	11.4	0.55	−0.54	4.79	4.0	−8.8	2.5
2.0	0.0	1.2	5.20	−0.50	0.70	38.2	−8.2	17.0
2.0	0.5	5.1	1.23	−0.56	1.95	9.0	−9.2	6.2
2.0	1.5	9.6	0.65	−0.56	3.94	4.8	−9.2	3.1

FIG. 4. Same as Fig. 2 but for $a = 0.5$ (dashed lines), $a = 1.0$ (solid lines), and $a = 1.5$ (dotted lines). In both plots, $\mu = 2.0$ and $\nu = N^2 = 1.0$.

it exhibited two extrema in y. In the present model we can find solutions whose cross-channel structure exhibits two, three, or more extrema depending on the choice of parameter values. In Figs. 9a–d we plot the upper-layer perturbation at $z = -1$, corresponding to the growth rate curves in Fig. 8. Clearly, the contour plot in Fig. 9a (i.e., the solution with the highest growth rate) shows anomalies with a single extremum in the y direction, such as those in Fig. 5. Figure 9b is the dipole mode, similar to the secondary mode in S91. Finally Figs. 9c and 9d show solutions with three and four extrema in the cross-channel direction, respectively.

As was already mentioned, our analysis shows that the number of solutions to the dispersion relation is dependent on μ. In Fig. 10 we graph $\sigma(k = 3.9)$ for all nontrivial solutions to (3.25) versus μ, where again $N^2 = \nu = a = 1.0$. We have chosen $k = 3.9$ since this is the fastest-growing wavenumber for the slowest-growing mode in Fig. 2a (dotted line). It is found that the system is stable to perturbations with this wavenumber for $0 < \mu < 0.6$, and a single solution mode appears at $\mu = 0.6$. Thereafter, additional modes appear at $\mu \approx$ 1.1, 1.8, 2.5, 3.2, and 4.0 with a total of six solutions at $\mu = 5.0$. We note that large values of μ are of little interest since we assumed that $\mu = O(1)$ in the derivation of (2.9)–(2.12). Increasing the buoyancy frequency N has a similar effect as increasing μ in that the number of unstable solutions to (3.25) also increases. This is again consistent with the idea that upper-layer stratification decreases the effective depth of the ambient fluid.

5. Numerical simulations

In this section we examine the long-term, nonlinear evolution of dense filaments and source flows numerically. For easy reference, our numerical experiments are divided into three groups, which we call case A, case B, and case C. Case A deals with the destabilization of an initial current whose configuration exactly corresponds to the assumptions in our linear theory. This is done as a check on the numerical scheme, and also allows a discussion of instability in the SOG. Case B describes the evolution of a dense plume that flows into the domain through one of the horizontal boundaries. The configuration of this set of simulations is similar to that of Jiang and Garwood (1996). As part of case B, we discuss the dependence of the flow features on the interaction parameter, μ. Finally, case C elucidates the role of bottom topography in the formation of coherent baroclinic vortex pairs. While cases A and B both employ a linearly sloping bottom, in case C we utilize a more realistic topography that is concave upward. All tests are performed in a rectangular domain $\Omega = \Omega_h \times [-1, 0]$, where the horizontal domain Ω_h will be described for each case separately. The governing equations (2.9)–(2.12) are discretized on a regular grid and evolved forward in time using the leapfrog method with a Robert-type filter (Asselin 1972) to damp out the time-splitting instability, and the Arakawa (1966) scheme employed for the Jacobian terms. The upper-layer streamfunction is recovered from the potential vorticity via a three-dimensional multigrid elliptic solver (Adams 1989). In the case of a periodic channel domain (case A), no-normal-flow conditions are applied on the channel walls. The source flow simulations, case B and case C, are performed in a closed domain with no-normal-flow conditions applied on all horizontal boundaries except at the plume source.

To facilitate discussion of the instability energetics, we define the upper-layer total energy,

$$E(t) = \frac{1}{2} \iiint_\Omega \boldsymbol{\nabla}\varphi \cdot \boldsymbol{\nabla}\varphi + \left(\frac{\varphi_z}{N}\right)^2 dx\, dy\, dz. \quad (5.1)$$

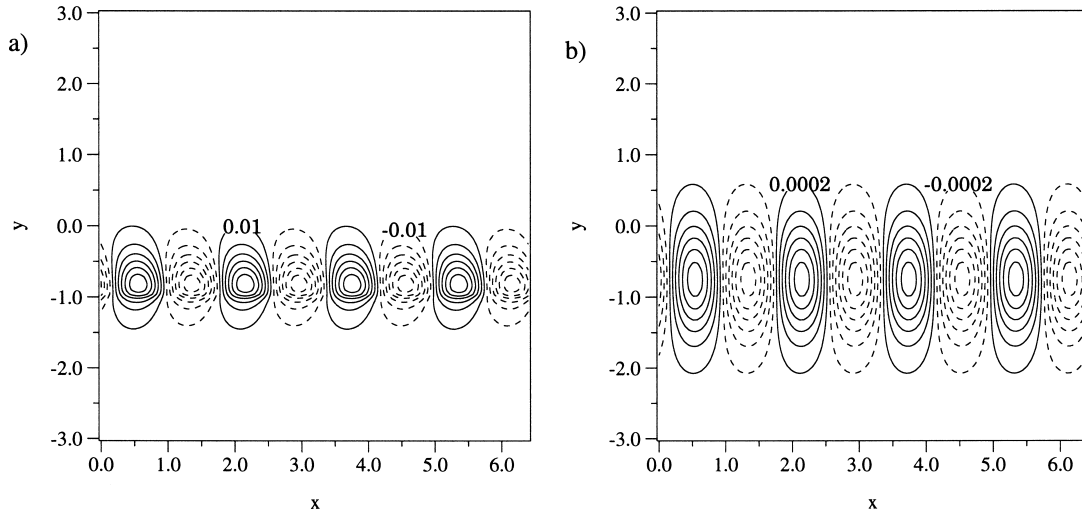The total lower-layer potential energy is given by

FIG. 5. Perturbation solution—that is, the upper-layer streamfunction—at (a) $z = -1$ and (b) $z = 0$, corresponding to the primary mode of instability for $\mu = N^2 = \nu = a = 1.0$, plotted at the most unstable wavenumber, $k = 3.9$ (see the dotted curve in Fig. 2a). Four along-channel wavelengths are shown. Dashed lines correspond to negative values. The contour interval is 1×10^{-2} in (a) and 2×10^{-4} in (b).

$$\mathrm{PE}_{\mathrm{total}}(t) = \frac{1}{2} \int\!\!\int_{\Omega_h} \left(h + \frac{h_B}{\mu} \right)^2 - \left(\frac{h_B}{\mu} \right)^2 dx\ dy; \quad (5.2)$$

however, the only time-dependent part of this quantity is the gravitational potential energy,

$$\mathrm{PE}(t) = \frac{1}{\mu} \int\!\!\int_{\Omega_h} h_B h\ dx\ dy. \quad (5.3)$$

The above quantities are directly related to the Hamiltonian structure associated with the governing equations, which is discussed more fully in PSa. $\mathrm{PE}(t)$ is released as dense fluid gradually slumps downhill and, without an initial mean flow in the upper layer (as is the case in this study), is the only source of available energy in this model. Similarly, starting with a quiescent upper layer, $E(t)$ tracks the growth of upper layer anomalies that result from the release of $\mathrm{PE}(t)$.
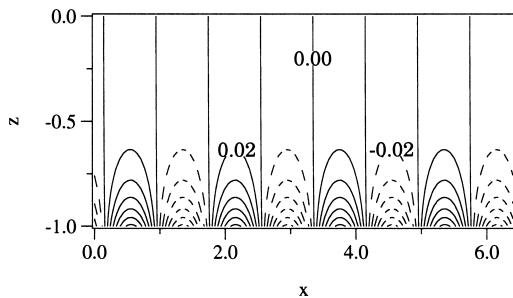

FIG. 6. Vertical cross section of the perturbation solution at $y = -0.84$, corresponding to the primary mode of instability for $\mu = N^2 = \nu = a = 1.0$, plotted at the most unstable wavenumber, $k = 3.9$ (see the dotted curve in Fig. 2a). Four along-channel wavelengths are shown. Dashed lines correspond to negative values. The contour interval is 2×10^{-2}.

a. Case A

Case A is performed in a periodic channel that allows four wavelengths of the most unstable mode (as in Figs. 5 and 6) with linearly sloping topography given by (3.12). The current profile is given by (3.19) with $a = 1.0$. For the parameter values $\mu = \nu = N = 1.0$, we obtain a horizontal domain $\Omega_h = \{(x, y) \mid 0 < x < 0.644, -3.0 < y < 3.0\}$. Initially the upper layer is seeded with a random superposition of waves such that the range of along-channel wavenumbers is centered on the most unstable mode, $k = 3.9$. The initial perturbation has no vertical variation, and the structure which later develops is purely due to the baroclinic dynamics of the instability. The initial perturbation amplitude is adjusted so that its energy is small in comparison with the lower-layer gravitational energy, that is, $E(0) = 10^{-30}\ \mathrm{PE}(0)$. This ensures that the dominant mode emerges before the flow leaves the linear regime. The grid resolution is $138 \times 128 \times 16$. Numerical friction is not employed in this simulation.

The instability is found to proceed according to our linear theory. Localized cyclonic/anticyclonic upper-layer pressure anomalies develop over the downslope incropping, and the incroppings themselves become deformed. Figure 11 shows the $z = -1$ and $z = 0$ cross-sections of the upper-layer streamfunction at $t = 15.0$, which is well within the linear regime (see Fig. 12). Comparing the contour plots in Figs. 11 and 5, it is clear that the horizontal structure of the perturbation is well described by our theory. While not shown, the vertical structure of upper-layer anomalies, which are in effect amplifying topographic Rossby waves, is found to be vertically tapered, as in Fig. 6. Deformation of the up-slope incropping is very small, whereas on the down-
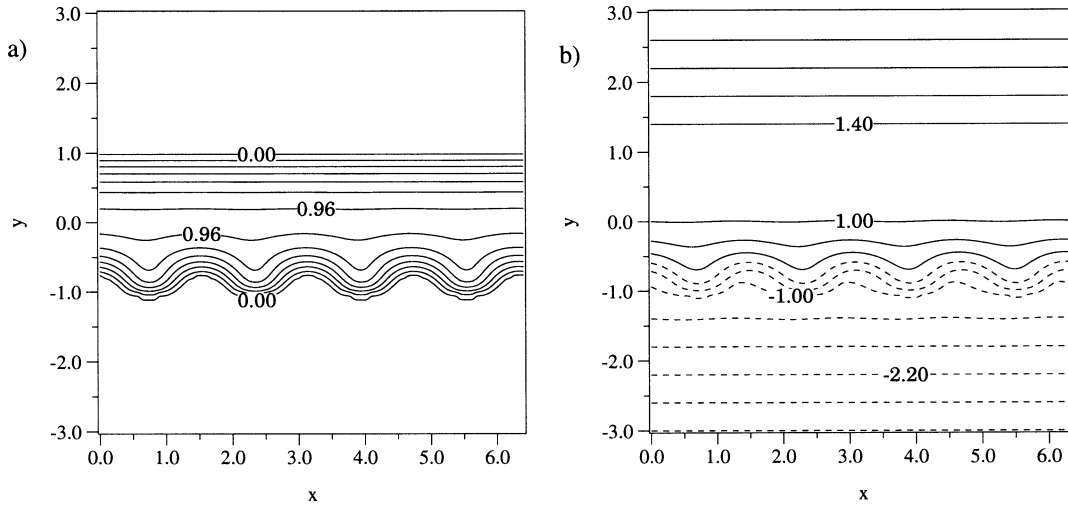
FIG. 7. Lower layer (a) thickness and (b) geostrophic pressure, corresponding to the primary mode of instability for $\mu = N^2 = \nu = a = 1.0$, plotted at the most unstable wavenumber, $k = 3.9$ (see the dotted curve in Fig. 2a). Four along-channel wavelengths are shown. Dashed lines correspond to negative values. The contour interval is 0.12 in (a) and 0.4 in (b).

slope side the current clearly exhibits the initial stages of plume formation, in agreement with Fig. 7a. Heuristically, local increases in lower-layer thickness lead to compression of upper-layer fluid columns causing anticyclonic anomalies. Similarly, regions of decreasing lower-layer thickness correspond to cyclonic upper-layer anomalies. The along-channel phase speed of the disturbance was approximately -0.61, which is consistent with the linear prediction (see Table 1). The initial flow evolution is similar to that observed in numerical sim-
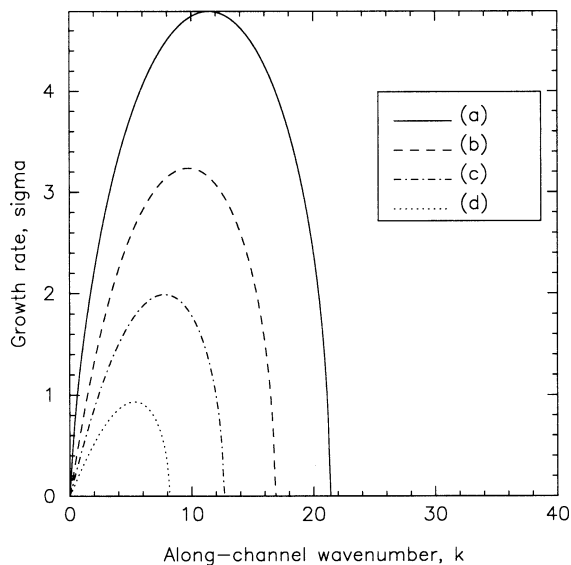

FIG. 8. Growth rates for four distinct solutions of (3.25) vs k, with $\mu = 3.0$ and $N^2 = \nu = a = 1.0$. Curve (a) (solid line) corresponds to the dashed line curve in Fig. 2a (i.e., the primary mode). Curves (b), (c), and (d) (i.e., secondary modes) have successively smaller maximum growth rates as well as high-wavenumber cutoffs.

ulations of Jungclaus et al. (2001). In their study of DSO dynamics using a primitive equation model, they found that anticyclones form closer to shore than cyclones. This behavior does not occur in the linear stage of growth that we are describing; however it does become apparent later in the simulation. The staggered vortex pattern also develops early in our source-flow simulations, described in the next section.

In Fig. 12 we plot the growth rate $\overline{\sigma}$ versus nondimensional time, where $\overline{\sigma}$ was calculated at each time step according to the finite-difference analog of

$$\overline{\sigma} = \frac{1}{2} \frac{d}{dt} \ln \frac{E(t)}{E(0)}. \qquad (5.4)$$

After an initial adjustment period, the growth rate levels off at a value of 1.36, which is reasonably close to the predicted growth rate of 1.42 (see Table 1). The system is in the linear regime for $5 \lesssim t \lesssim 25$, after which nonlinear effects become important. Although not shown, at this point the cross-slope extent of lower-layer plumes is on the order of a, the current half-width, and the current is still mostly intact. The instability is nonlinearly saturated, temporarily halting the growth, and the growth rate remains close to zero for $30 \lesssim t \lesssim 50$. Further nonlinear evolution of the flow has been described in RS (see also Swaters 1998), however a few remarks are appropriate here. The upper layer in this model is governed by QG dynamics, and is therefore subject to the red energy cascade (Pedlosky 1987). Typically, we find that after the initial saturation, upper-layer anomalies begin to merge, and the dominant along-channel wavenumber of the instability decreases. A similar drift toward larger length scales is then induced in the lower layer, and growth resumes at the lower wavenumber.
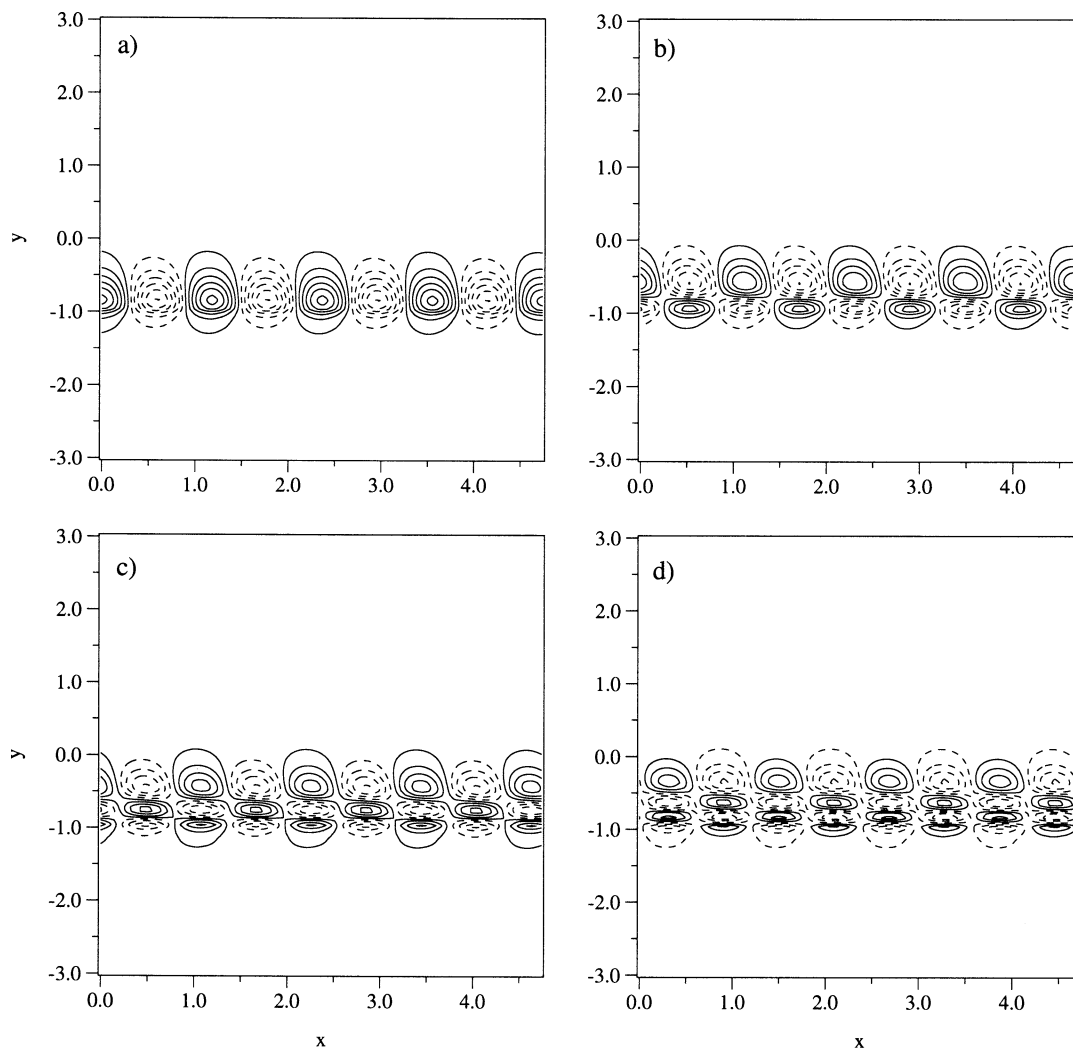
FIG. 9. Contour plots of the perturbation at $z = -1$ with the parameter values $\mu = 2.0$, $N^2 = 1.0$, and $\nu = a = 1.0$ at $k = 5.3$. The plots (a), (b), (c), and (d) correspond to the curves (a), (b), (c), and (d) in Fig. 8. The wavenumber $k = 5.3$ is the most unstable wavenumber for the smallest growth rate curve shown, i.e., curve (d) in Fig. 8. Dashed lines correspond to negative values.

By contrast, no such shift in wavelength is evident in simulations of propagating plumes as in case B, described below. In that scenario, mushroom-shaped subplumes form at a frequency roughly consistent with our linear theory, and the original plume disintegrates before any shift in lengthscale is observed. The source-flow configuration (cases B, C) is more relevant for DSO dynamics than that of a continuous filament (case A), and it will be discussed fully in sections 5b and 5c. Finally, we note that the behavior we observed in case A is somewhat different from that presented in Swaters (1998). As the linear regime in the limit of a homogeneous upper layer is characterized by longer length scales in both the alongslope and cross-slope directions, developing pressure anomalies typically extend over the entire width of the current. This results in fairly prominent deformations of both incroppings (the sinuous

mode: see S91) and sustained growth at the original wavenumber, which breaks up the mean flow into discrete spiral features.

Fully nonlinear simulations of an evolving isolated front along a generic valleylike topography, in rough approximation of SOG bathymetry, were described by RS. Indeed, their integrations using the PSa equations showed rapidly growing bottom-intensified eddy features associated with the slumping of dense fluid, which were highly localized in space, unlike the broad, height-independent eddy anomalies in KST. The mean flow in the dense layer was eventually broken up and did not evolve into any recognizable, coherent features. Because of interaction with the opposite slope, as well as the upscale energy cascade inherent in the equations, the final flow was an irregular cyclonic gyre with numerous filaments. These finescale structures could potentially
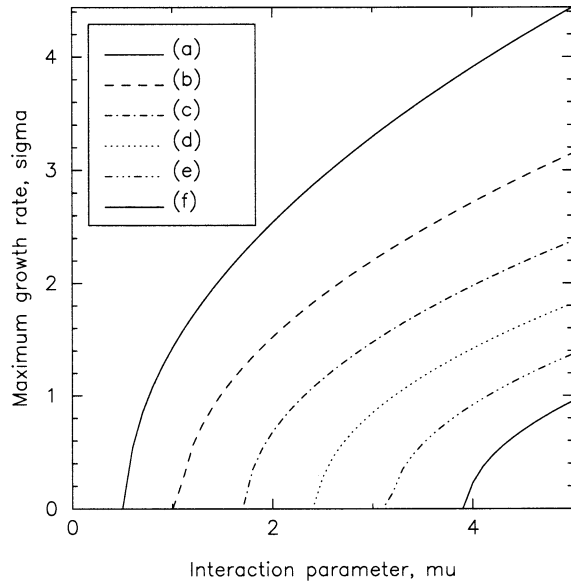
FIG. 10. Growth rate at $k = 3.9$ vs μ for all existing unstable modes. This wavenumber is the most unstable wavenumber for the slowest-growing solution in Fig. 2a (dotted-line curve). All curves in this plot correspond to $N^2 = \nu = a = 1.0$.
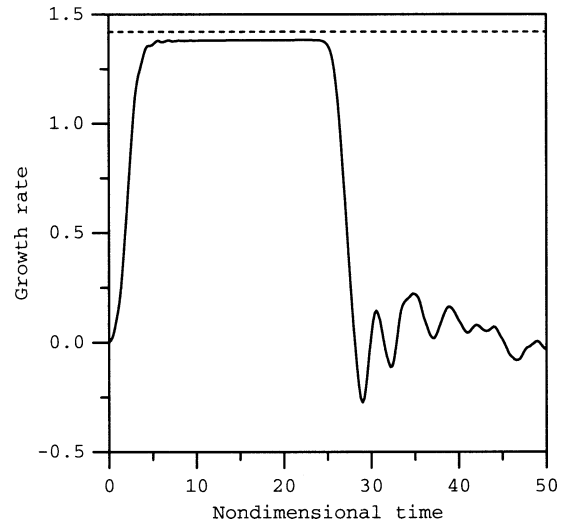

FIG. 12. Computed perturbation growth rate vs time (solid line) for the numerical simulation in case A. The growth rate is based on the upper-layer total energy (5.1). The flat portion of the curve between $t \approx 5.0$ and $t \approx 25.0$ corresponds to the regime of linear growth, where our analysis applies. The dotted line shows the theoretical growth rate, 1.42.

explain the velocity fluctuations reported by (Stacey et al. 1991). Some current meter measurements also indicate the presence of a cyclonic, basinwide gyre at middepth; however, more data would be required before any conclusions should be drawn in this respect.

b. Case B

An *x*-invariant dense filament in a periodic channel is obviously a convenient steady-state solution for the purposes of linear analysis. Our discussion of instability

in this context also facilitated comparison with earlier studies. However, dense water intrusions tend to be pulselike or episodic rather than continuous. Moreover, laboratory experiments of bottom-water spreading usually involve source flows with no imposed periodic structure. Nevertheless, we find that the linear instability characteristics derived in section 4 remain valid, to a reasonable degree, for unsteady, propagating plumes. Case B differs from case A in that the domain is closed, and the dense fluid enters from a source region along one of the boundaries. As part of case B, we will also investigate the effect of varying the interaction param-
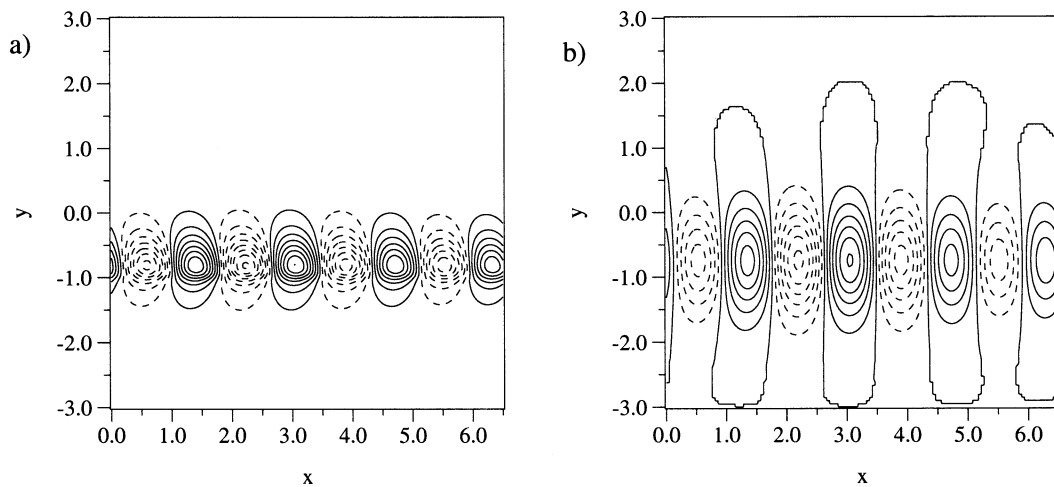

FIG. 11. Contour plots of the upper layer streamfunction at (a) $z = -1$ and (b) $z = 0$, obtained from the numerical simulation in case A, at $t = 15.0$. This figure should be compared with Fig. 5. The contour extrema and intervals are (a) -1.05×10^{-2}, 1.05×10^{-2}, 1.4×10^{-3}; and (b) -2.4×10^{-4}, 2.4×10^{-4}, 4.0×10^{-5}, respectively. Dashed contours correspond to negative values.

TABLE 2. Dimensional overflow properties and instability characteristics for case B: u_u and u_d refer to the inflow velocity at the upslope and downslope incropping, respectively. Other symbols are defined in the text. Values of λ^*, T^*, and T_e^* are those predicted by the linear theory for $\nu = N^2 = 1.0$ and $a = 2.5$ (appropriately scaled for the DSO) and are consistent with the results of the nonlinear source-flow simulations.

Case	μ	h_* (m)	Q (Sv)	u_u (cm s^{-1})	u_d (cm s^{-1})	λ^* (km)	T^* (days)	T_e^*
B1	1.0	200	2.0	−6	−54	29	1.6	11 h
B2	0.50	100	1.0	−18	−42	42	1.9	18 h
B3	0.25	50	0.5	−24	−36	48	2.1	1.2 day
B4	0.10	20	0.2	−28	−32	52	2.1	2.1 day

eter, μ. The standard experiment is case B1, with $\mu = 1.0$. Case B2 ($\mu = 0.5$), B3 ($\mu = 0.25$), and B4 ($\mu = 0.1$) will be described below. For application to the DSO, we introduce the following parameter values, where the notation is the same as in section 2: $H = 900$ m, $s^* = 0.02$, $g' = 2.0 \times 10^{-3}$ m s^{-2}, $f_0 = 1.3 \times 10^{-4}$ s^{-1}, and $N_* = 1.5 \times 10^{-3}$ s^{-1}. This determines the stratification number, $N = 1.0$, and slope parameter, $s = 0.22$. We also obtain the dynamic length scale, $L^* = 10$ km, lower-layer velocity scale, $U_2 = 30$ cm s^{-1}, and with $\delta = 0.22$ (as in the standard experiment), an upper-layer velocity scale of $U_1 = 30$ cm s^{-1}. Dimensionally, the computational domain covers an area of 320 km $\times$ 192 km, with a grid resolution of 1 km. Employing 16 vertical levels, the upper-layer vertical resolution is 60 m. The time scaling is 10 h and the dimensional time step is 5.5 min. In order to damp out grid-scale noise, Laplacian and biharmonic numerical friction are introduced into the lower-layer equation with coefficients 5.0 $\times$ 10^{-3} and 5.0 $\times$ 10^{-4}, respectively.

A source of dense water is maintained on the right boundary at $y = 144$ km for the duration of the experiment by imposing a fixed, parabolic profile on h, the lower-layer thickness. This is the same profile as the basic state (3.19) with $a = 2.5$ but is shifted in the y coordinate and applied at the boundary only. Leading-order geostrophy then induces a velocity in the negative x direction, forcing fluid into the domain at a constant rate. The current is 50 km wide and has a thickness of 200 m in the standard experiment (see Table 2). We note that there is no upslope countercurrent associated with this thickness profile. The volume transport Q into the domain is then 2.0 Sv, which is a reasonable approximation for the DSO (Price and Baringer 1994). In order to avoid steep spatial gradients at the head of the current, a surface in the shape of a quarter-sphere is also initially imposed adjacent to the source region, as shown in Fig. 13a. However, this ad hoc measure plays a minor role in subsequent dynamics, and its presence or neglect does not significantly alter the results. We initialize the upper-layer streamfunction to be identically zero and prescribe no-normal-flow conditions on all the horizontal walls. A uniformly distributed mass sink in the upper layer compensates for the lower-layer flux. In order to avoid reflection of Rossby waves, a smoothing operator is successively applied to the upper-layer streamfunction

at the sidewalls and downstream boundary. This crude sponge effectively removes energy from the system and allows us to focus on dynamics in the interior of the domain.

The evolution of the lower-layer height, $h(x, y, t)$, for case B1 is shown in Fig. 13 at 0, 1.6, 3.2, and 4.8 days. Corresponding plots of the upper-layer streamfunction at the surface, $\varphi(x, y, 0, t)$, are shown in Fig. 14. The computational domain in case B and case C was quite long to ensure that instability in the source region was not influenced by the downstream boundary. In order to focus on the unstable plumes, the panels in Figs. 13 and 14 only show the rightmost 192-km segment of the domain. The current becomes unstable immediately after entering the domain and a descending, mushroom-shaped plume has formed at 1.6 days. It continues to deform as it propagates along and down the slope, while two more plumes appear in the next two plots, at day 3.2 and 4.8, respectively. For a parabolic current with $a = 2.5$, our linear analysis suggests a frequency of 1.57. This yields a dimensional period of roughly 1.6 days, which is indeed the period between successive subplumes in this simulation. The agreement in plume frequency, and therefore eddy size, seems to be a robust phenomenon. Thus, we feel that the linear results of section 4 are useful in characterizing the development of source flows in this regime. Good correlation between the predicted and actual frequencies of instability events is, to some degree, a result of the simplified physics that we have assumed. To illustrate, as μ is decreased and the instability becomes weaker, the geostrophically balanced plume travels along the slope and acts similarly to the periodic gravity currents our linear theory considers. Table 2 lists some characteristics of the instability in dimensional units, as predicted by the analysis of section 4. The period, T^*, increases as μ (equivalently, the current height) decreases.

As part of the baroclinic process, strong eddies of both signs develop in the upper layer and migrate away from the source region as seen in Figs. 14b–d. These vortices are bottom intensified, although their surface signature is reasonably strong. Typical velocities are 120 cm s^{-1} at the bottom and 50 cm s^{-1} at the top of the layer. Overall, we did not find cyclones to be stronger than anticyclones in our simulations. At times, we observed domes of dense fluid coupled to strong low-
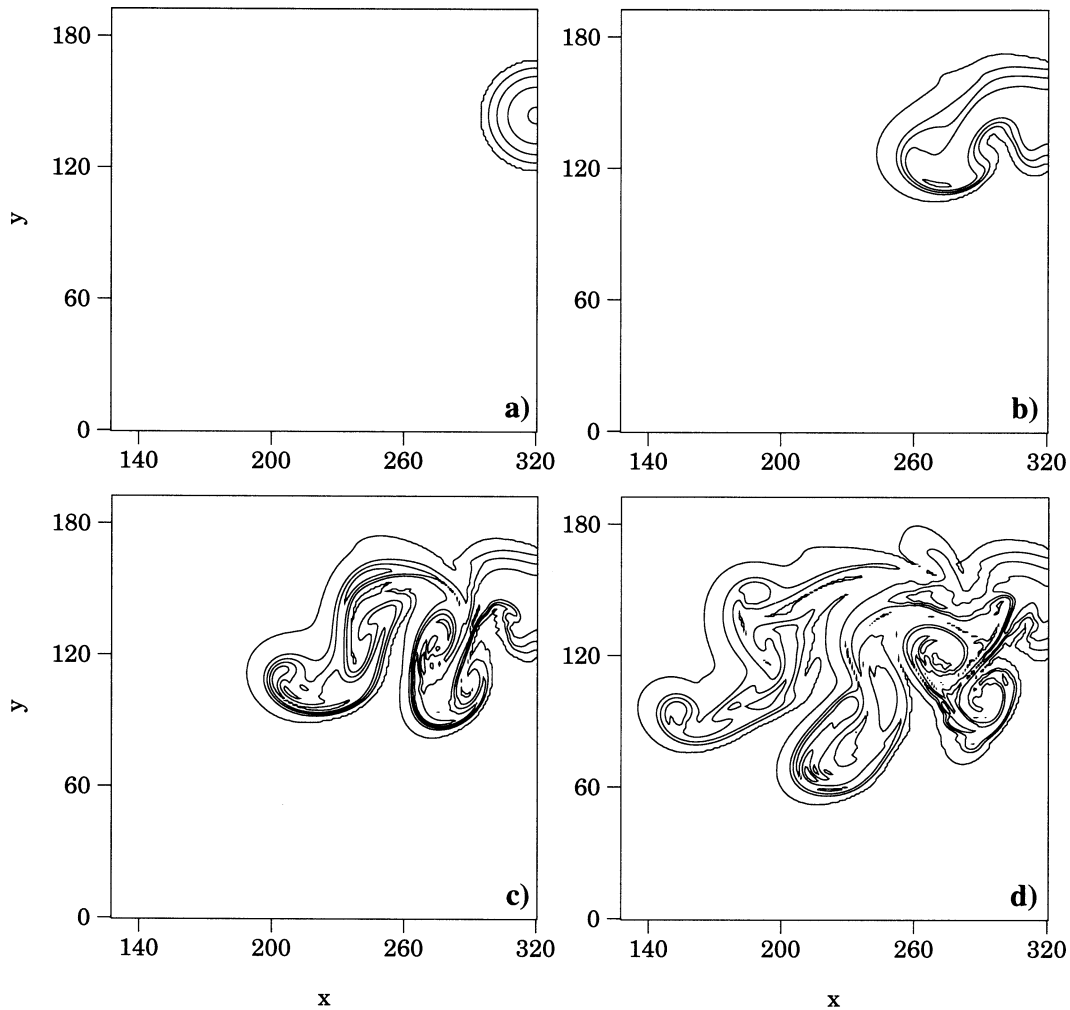
FIG. 13. Contour plots of the dimensional lower layer thickness at (a) 0, (b) 1.6, (c) 3.2, and (d) 4.8 days for the simulation in case B1. The contour extrema and intervals are (a) 0, 200, 50 m; (b) 0, 200, 50 m; (c) 0, 240, 60 m; and (d) 0, 240, 60 m, respectively.

pressure anomalies in the ambient layer, not unlike the vortices described by Whitehead et al. (1990) and Lane-Serff and Baines (1998, 2000). However, these baroclinic pairs did not form with any regularity and were not very long-lived (but see the discussion in section 5c). As the above authors have noted, there are several potential processes by which a plume wraps up into a coherent, domed anomaly, and at the same time becomes coupled to a strong cyclone in the overlying fluid. Mechanisms such as Ekman draining and geostrophic adjustment, suggested by Lane-Serff and Baines (1998), are absent in our model. Krauss and Käse (1998) argue that ageostrophic advection of positive vorticity into the core of the eddy plays an important role in cyclogenesis. In the PSa formalism, the only contribution from the lower-layer momentum equation is the geostrophic relation (the so-called planetary geostrophic approximation), while the upper layer is governed by the conservation of QG PV. Upper- and lower-layer relative vor-

ticity is advected solely by the geostrophic velocity field, which may explain the scarcity of baroclinic vortex pairs in our tests. However, coherent structures of this sort do appear regularly in case C, where the topography is no longer linear. It must also be remembered that we have chosen very simple boundary conditions with no inflow or outflow imposed on the upper-layer velocity. Nevertheless, we found a definite asymmetry in the location of the eddies, in that cyclones tended to form on the offshore side of the current, while anticyclones appeared closer to shore. While this behavior is not described by our linear theory, it is entirely consistent with the numerical findings of Krauss and Käse (1998) and Jungclaus et al. (2001), as well as the observational data presented in Krauss and Käse (1998).

The propagation of subplumes along and down the slope is associated with very regular velocity fluctuations in both layers. In Fig. 15a, for instance, we plot the cross-slope average of the cross-slope velocity ver-
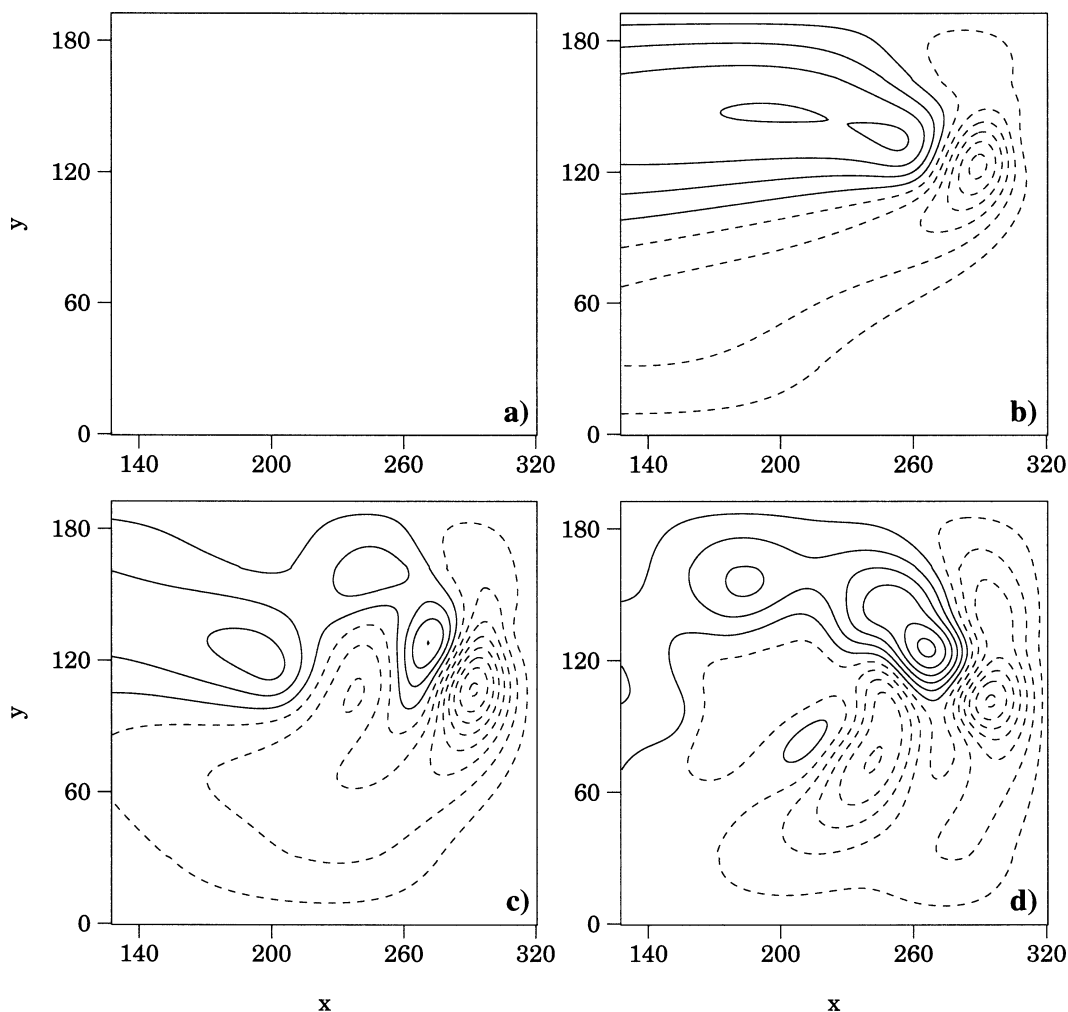
FIG. 14. Contour plots of the nondimensional upper-layer streamfunction at $z = 0$ corresponding to the plots in Fig. 13. Dashed contours correspond to negative values. The initial condition (a) is zero everywhere. The contour extrema and intervals for the other plots are, respectively, (b) -1.1, 0.7, 0.2; (c) -2.3, 1.0, 0.3; and (d) -2.6, 2.2, 0.4. Dashed lines correspond to negative values.

sus time measured at $x = 270$ km, that is, 50 km downstream of the source. Both the upper and lower layer exhibit roughly sinusoidal velocity variations with an average period of 1.6 days. Similar fluctuations exist in the alongslope velocities (not shown). Near-bottom velocity fluctuations with timescales of 1.5–2.5 days downstream of Denmark Strait have been reported by several authors on the basis of current meter measurements (Dickson and Brown 1994). A good example is the dataset from the Anmagssalik array off the east coast of Greenland [Dickson and Brown (1994), their Fig. 6]. As μ decreases, we find that velocities in the lower layer tend to be weaker than those at intermediate depths. In Fig. 15b, we plot the evolving maximum lower-layer speed, $\sqrt{u_2^2 + v_2^2}$, for $\mu = 0.5$. The same figure also contains the upper layer maximum speed at $z = -1$ and $z = 0$ as a function of time. Velocities increase up to about 5 days, and thereafter the system remains in a

quasi-steady state until the plume reaches the downstream boundary at 10 days. As Fig. 15b suggests, the upper-layer velocity structure is bottom intensified, with speeds reaching 200 cm s^{-1} at the fluid interface during the first three instability events. However, lower-layer velocities during this time period rarely exceed 170 cm s^{-1}. Thus, in actual oceanographic applications, the highest velocities may occur not in the overflow waters but at some depth above the bottom. We note that these velocities are somewhat higher than those typically observed in the DSO; however, these are the maximum speeds and are limited to localized regions of the domain. During a typical instability event, we observe the following trend in the alongshore velocity. Initially the velocity of a nascent plume is close to the Nof velocity with little cross-slope motion. During instability the alongslope component significantly decreases and the cross-slope component increases. After saturation the
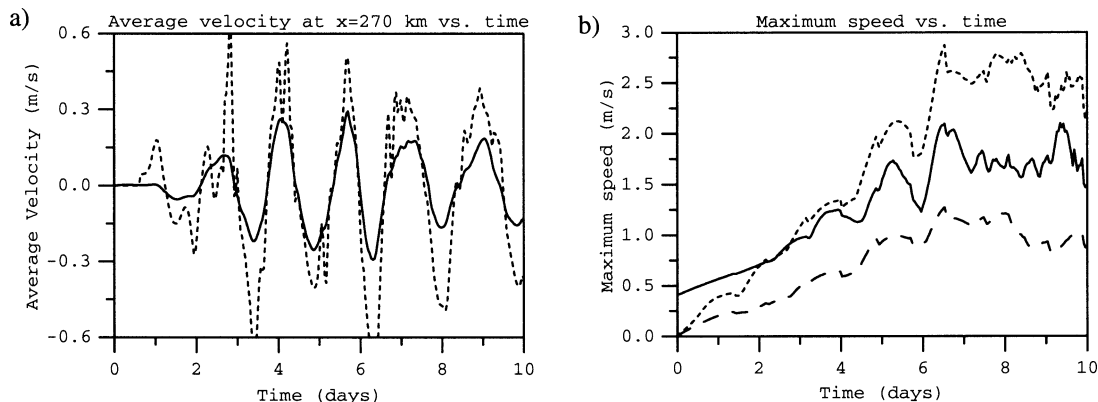
a)

b)

FIG. 15. (a) Cross-slope average of cross-slope velocity (m s^{-1}) vs time (days) measured 50 km downstream from the inflow for case B1. Continuous line refers to the lower layer, dotted line refers to the upper layer at $z = -1$. (b) Maximum flow speed (m s^{-1}) over the domain vs time (days) for case B2. Speeds for the lower layer (solid line), upper layer at $z = -1$ (dotted line), and upper layer at $z = 0$ (dashed line) are shown.

newly-formed plume resumes alongslope motion at the Nof speed.

The dynamics of the instability is highly dependent on the parameter μ, which measures the relative size of the upper- and lower-layer Rossby numbers. This parameter was recently used by Etling et al. (2000) to characterize the regime of instability in the DSO.[1] Here we present three additional simulations that demonstrate the influence of μ on plume penetration and maximum velocities. The simulations are the same as case B1 in every respect except for the value of μ. Lower values of the interaction parameter may be interpreted as a smaller current height. The volume flux at the Denmark Strait sill is known to be quite variable in time (Bruce 1995), so the effect of a weaker source is of interest. For reference, Table 2 lists the four cases, along with the corresponding current height h_*, source strength Q, as well as the minimum and maximum velocity at the source. As discussed in the appendix, the mean current velocity at the inflow is 30 cm s^{-1}, that is, the Nof speed. The theoretical wavelength λ^*, period between instability events T^*, and e-folding time T_e^* for these simulations are also given in Table 2. Qualitatively, the trend in T_e^* and T^* implies that the instability should be faster and more intense for higher values of μ. This is indeed the case in our simulations.

Figure 16 is a plot of plume penetration distance versus time for the four different values of μ. We define this distance as the smallest y coordinate over the domain for which h is nonzero. Initially, the downslope incropping is located at $y = 119$ km for all four cases. In case B1, some subplumes reach the downslope

boundary, $y = 0$, at 8 days. As we would expect, smaller values of μ induce a weaker instability, allowing the plume to propagate farther along the topography as a coherent current. Conversely, more vigorous plume formation events resulting from higher values of the interaction parameter lead to increased cross-slope (and therefore downslope) motion. Kinks in the curves, most visible in the $\mu = 1.0$ case, correspond to temporary saturation of growing subplumes. It should be noted that, once formed, some of the subplumes deform and subsequently undergo further baroclinic instability.

Eddy formation in the DSO has been the focus of many recent modeling efforts. Spall and Price (1998) propose the following mechanism by which strong cyclones are produced at regular intervals south of the strait. In their theory, dense fluid descends into the deeper ocean due to bottom drag without the need for in-
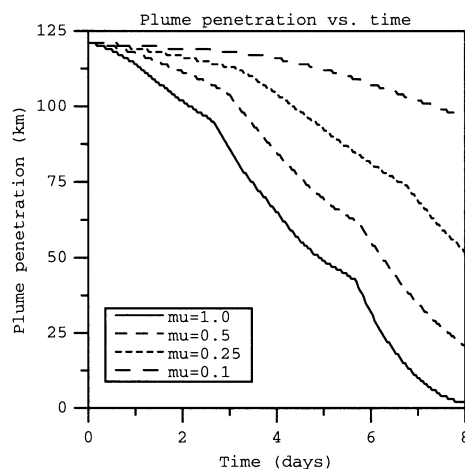

FIG. 16. Plume penetration (km) vs time for the simulations in case B. Plume penetration refers to the smallest y coordinate for which $h(x, y, t) > 0$. Initially, the downslope edge of the plume is at $y = 119$ km in all four cases. The cross-slope extent of the plume decreases with μ since the instability becomes progressively weaker.

[1] Etling et al. (2000) estimate that $\mu = 0.6$ in the DSO, which is in the transition region between the vortex regime (lower μ) and plume regime (higher μ). Note, however, that this does not imply that our simulations describe the vortex regime since our derivation of the governing equations assumed that the fluid is geostrophic to leading order.

stability. Their simulations suggest that the overflow water piles up near the sill, causing an alongslope density gradient which then induces midlevel water to migrate offshore, as required by the thermal wind relation. The intense stretching of the upper Arctic Intermediate Water then leads to pronounced cyclonic eddies. However, Krauss and Käse (1998) point out that observations do not seem to support the presence of this intermediate layer farther than 150 km from the sill, or its stretching to any significant degree.[2] Jungclaus et al. (2001) suggest that the mechanism of Spall and Price (1998) may be operative if the local Rossby number is $O(1)$, while for smaller Rossby numbers baroclinic instability of the deep layer induces eddies of both signs to form in the ambient ocean. Indeed, observations from the R/V *Poseidon* cruise in 1996 do confirm the existence of anticyclones in the DSO region (Krauss and Käse 1998). On theoretical grounds, Etling et al. (2000) argue that the dynamics of the DSO lies somewhere between these two regimes. It is possible therefore, that both of the mechanisms described above are operative to some degree in the DSO and other overflows. Since the PSa model is derived assuming geostrophy to leading order, our simulations are relevant for the small Rossby number regime and are in that respect similar to the numerical results of Jiang and Garwood (1996) and the second series of laboratory experiments in Etling et al. (2000). We would also like to make a general remark regarding cyclone intensification. Given that the Denmark Strait outflow encounters increasingly deeper topography upon entering the Irminger Basin, we should expect that fluid columns tend to be stretched rather than compressed. It seems reasonable that, on average, this trend leads to a net gain in positive PV, which may then be manifested in subsequent instability processes.

c. Case C

While eddies of both signs have been reported in association with the DSO, observations and numerical results suggest that intense cyclones dominate the flow field (Bruce 1995; Jungclaus et al. 2001). Baroclinic vortex pairs with a strong cyclonic component were observed in the laboratory by Whitehead et al. (1990), Lane-Serff and Baines (1998), and others. Such vortices exhibit a coherent dome of dense fluid, coupled to a low-pressure anomaly in the overlying water. They travel along the slope as a unit, often for a significant distance. Poulin and Swaters (1999b) found analytical, radially symmetric eddy solutions to (2.9)–(2.12) with exactly these characteristics. For a lower-layer anomaly with a parabolic cross section, the upper-layer stream-

---

[2] On the other hand, some observations do show midlevel water in the cores of the cyclonic eddies (e.g., Fig. 2 in Spall and Price 1998) downstream of the sill. Midlevel fluid in the surrounding ocean could be difficult to detect because of intense mixing associated with eddy formation (M. Spall 2002, personal communication).

function could be described in terms of a superposition of Bessel functions. It was found that these eddies were bottom-intensified, and could transport fluid parcels for physically relevant values of the parameter μ. In addition, the cyclonic circulation in the upper layer was typically strong enough to reverse the anticyclonic flow in the core of the dome anomaly. We believe this property to be an important factor in the coupling of the two layers. Our simulations in case B, which employed linearly sloping topography, did not give rise to such eddy pairs with any regularity. On the other hand, we have found that topography that is concave upward does allow for the formation of these features at regular intervals. Coastal topography, such as the western boundary of the Irminger Basin, is often steeper near the coast than offshore (e.g., Bruce 1995). Indeed, we can expect the bathymetry of any oceanic subbasin to flatten out in its interior. Therefore, we feel that a discussion of the effects curvature in the topography is relevant here.

Let us consider a geostrophically balanced abyssal current with thickness $h(y)$ situated on topography given by $z = h_B(y)$ (the case of a linearly sloped bottom is sketched in Fig. A1). For simplicity, let $\mu = 1.0$, in the language of section 2. Assuming that the overlying fluid is initially quiescent, the lower-layer pressure (2.15) simplifies to

$$p = h_B + h. \quad (5.5)$$

Given that $p(y)$ is a streamfunction and the velocity is geostrophic, the lower-layer relative vorticity ζ will be

$$\zeta = (h_B + h)_{yy}. \quad (5.6)$$

If h_B is linear in y, the topographic term vanishes. Moreover, for any $h(y)$ that is concave downward (e.g., a parabolic profile), we can see that the current possesses anticyclonic shear as $\zeta < 0$. This inherent negative vorticity must be overcome by an upper-layer cyclone if the dense fluid is to wrap up into a coherent dome. However, if h_B is an increasing function of y, then the topographic term can compensate to some degree, decreasing the anticyclonic shear. In that situation, upper-layer cyclones that form as a result of the initial instability are more likely to be strong enough to advect growing plumes in a cyclonic fashion, thus leading to the baroclinic vortex pairs described above. This is the process we see occurring in case C.

The boundary source is placed with its center at $y = 115$ km, in the same domain as case B. We introduce nondimensional topography of the form

$$h_B = A \ln[\exp(y - y_0) + 1.0], \quad (5.7)$$

which has the property that its gradient vanishes for decreasing y (away from the shore) and approaches a positive constant for increasing y (close to shore). We choose $A = 1.1$ and $y_0 = 9.2$ so that the topographic slope is 0.02 (as in case B) at the plume center. The topography flattens out considerably just below the downslope incropping, where we expect plume devel-
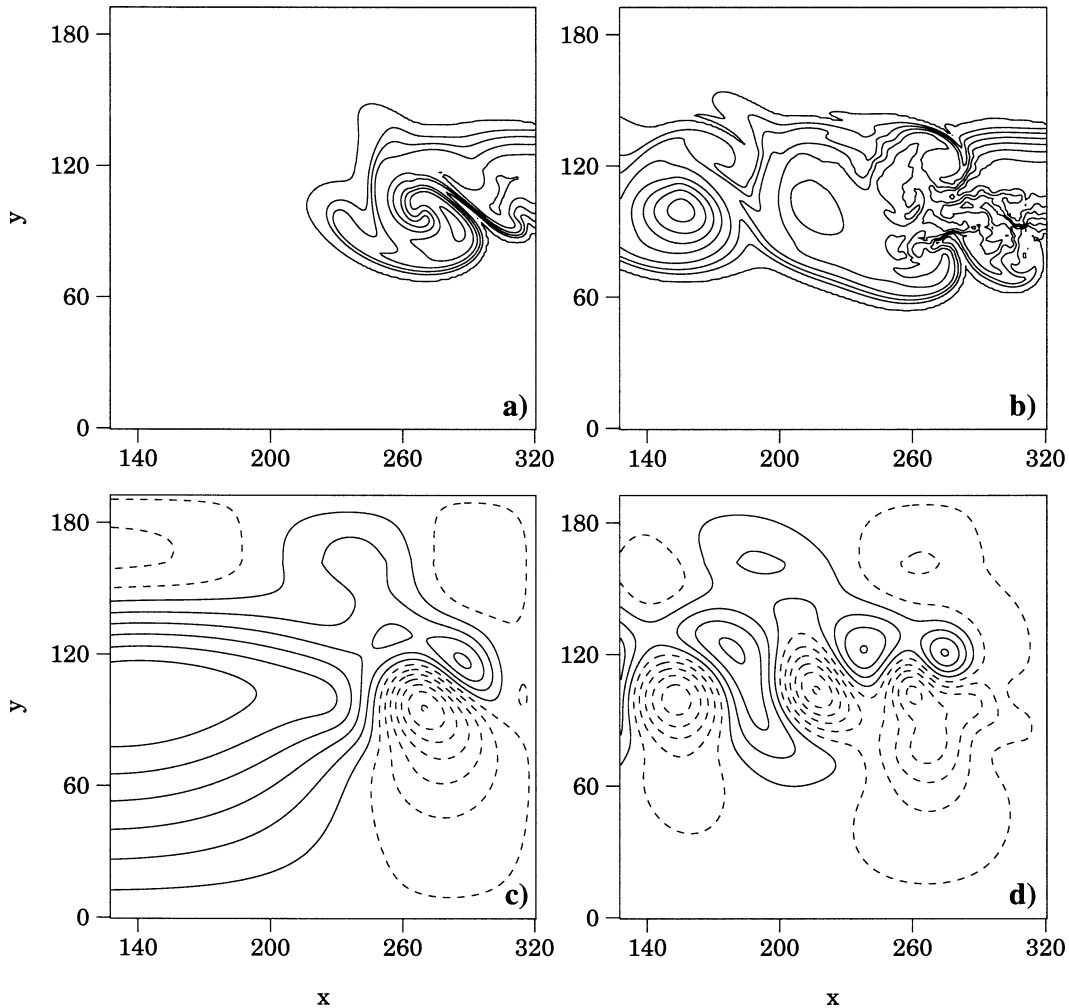
FIG. 17. Dimensional lower-layer thickness at (a) 3.0 and (b) 8.5 days, and nondimensional upper-layer streamfunction at $z = 0$ at (c) 3.0 and (d) 8.5 days, for case C. The contour extrema and intervals are, respectively, (a) 0, 200, 40 m; (b) 0, 240, 30 m; (c) -0.92, 0.88, 0.15; and (d) -0.63, 0.45, 0.12. Dashed lines correspond to negative values.

opment. Rayleigh damping of the form $-r\mathbf{u}_2$ has been introduced in the derivation of the lower-layer governing equation. This simple bottom drag was used by Samelson (1998) and Choboter and Swaters (2002, manuscript submitted to *J. Phys. Oceanogr.*), among others, and has the advantage that $\mathbf{u}_2$ can still be determined diagnostically from h. The modified equations (2.11) and (2.12) may then be written

$$(\varphi_z + N^2 h)_t + \mu J(\varphi, \varphi_z) + N^2 J(\varphi, h_B + \mu h) = 0$$
$$\text{on } z = -1, \qquad (5.8)$$

$$h_t + \frac{1}{r^2 + 1} J(\mu\varphi + h_B, h) = \frac{r}{r^2 + 1} \nabla \cdot (h \nabla p)$$
$$\text{on } z = -1, \qquad (5.9)$$

where p is given by (2.15). The diffusion-type term on the right-hand side of (5.9) may be interpreted as a crude parameterization for agoestrophic effects that have been

neglected in the model, and is conducive to the development of prominent domed features. However, we stress that curvature in the topography plays the dominant role in this process. We choose $r = 2.5 \times 10^{-2}$, although other values give similar results. The simulation is the same as case B in all other respects.

Initial flow fields are similar to Figs. 13a and 14a, and are not shown. Contour plots of the evolving plume for $t = 3.0$ and 8.5 days are displayed in Figs. 17a and 17b, respectively. Plots of the upper-layer streamfunction at $z = 0$ are displayed in Figs. 17c and 17d. We remind the reader that, as before, each panel only shows the rightmost 192-km segment of the computational domain. While the initial instability proceeds similarly to the previous experiments, at 3.0 days the plume begins to wrap up on itself in a cyclonic sense because of an intense low pressure cell in the overlying fluid (Fig. 17c). The result is a coherent dome of lower-layer fluid, seen on the left-hand side of Fig. 17b, coupled to the

cyclonic eddy visible in the same position in Fig. 17d. This dome–cyclone pair was observed to propagate in unison for a much greater distance than any anomaly in the previous simulations. As soon as the original dome had formed and moved away from the source, another one began to develop in a similar fashion, induced by another strong upper-layer cyclone. This pair, though less well defined, appears in the middle of Figs. 17b and 17d. The alongslope speed of the baroclinic vortices was approximately 22 cm s^{-1}, somewhat slower than the average speed of 27 cm s^{-1} exhibited by DSO eddies (Bruce 1995). A small but non-negligible downhill component was also consistently present in our tests. We note that the theoretical Nof speed of 30 cm s^{-1} for a slope, $s^* = 0.02$, is not inconsistent with available data on cyclone propagation in the DSO.

The dome–cyclone coupling is more clear from a movie of the simulation than the contour plots in Fig. 17. Obviously, the instability gives rise to other pressure anomalies; however, we find these to be more elongated and transient, and usually weaker than the paired cyclones. We are able to discern a third baroclinic vortex at 8.5 days; however, by this time the flow at the source is highly irregular. The reason for this is that the flow is geostrophic and unstable as soon as it enters the domain. However, as noted previously, each baroclinic event is associated with a local decrease in the alongslope speed. The result is that dense fluid temporarily piles up behind each developing dome with no clear outlet. This behavior is a consequence of the simplifying assumptions made in deriving the governing equations. The primitive equation numerical model of Jiang and Garwood (1996) allowed for downslope motion before geostrophic adjustment took place, and their source was located at the top of the slope, providing a buffer zone between the source and the unstable region. Naturally, laboratory experiments, such as those of Lane-Serff and Baines (1998) or Etling et al. (2000), allow for several types of sinks for the dense fluid, including Ekman draining and turbulent entrainment. Nevertheless, the process we have described here is robust with respect to the parameters A, y_0, and r. The only crucial ingredient is topography whose gradient increases with y.

The topography in case C was similar enough to the linearly sloping bottom used previously that the frequency of instability events did not change significantly. On average, the separation between cold dome anomalies was about 60 km, which is not unreasonable compared to eddies in the DSO. Each upper-layer cyclone had a diameter of roughly 35 km, which agrees well with observational estimates of 30 km (e.g., Bruce 1995). Undoubtedly, the dynamics that we have presented reflect only some aspects of instability in abyssal currents. Nevertheless, the basic mechanisms we described should be relevant for the DSO and other rotationally dominated overflows. We are not claiming that the topographic effect can, by itself, account for the particular intensity of cyclogenesis in the DSO. The

western slope of the Irminger Basin does not seem to be significantly different from the bathymetry south of the Iceland–Faroe Ridge, for example. A detailed comparison of the topography in several overflow regions, together with knowledge of the exact overflow paths, could certainly shed light on this issue.

6. Conclusions

We have developed a linear instability theory for the baroclinic model of Poulin and Swaters (1999a), which describes abyssal currents in a continuously stratified ocean. The instability characteristics associated with a parabolic abyssal current in the presence of linearly sloping topography were not inconsistent with observations of variability in the Strait of Georgia and the Irminger Basin. The spatial structure of the perturbation was shown to exhibit pronounced deformations of the dense fluid on the downslope side, as well as eddies of both signs in the overlying ocean. This behavior is similar to the initial stages of instability in primitive equation numerical studies such as Jungclaus et al. (2001) and observed flow fields in the Denmark Strait overflow region (Krauss and Käse 1998). Secondary modes of instability, similar to those discussed in Swaters (1991), were found for physically relevant values of μ. Numerical simulations confirmed the linear results, but also suggested that the nonlinear evolution of a continuous filament is not reflective of source flow instabilities in this dynamical regime, due to the red energy cascade.

We found that the frequency and form of the instability predicted by our linear analysis is useful in characterizing the development of plumes originating at a boundary source. Our numerical tests showed that the plume evolution is similar to that reported by Jiang and Garwood (1996) and Etling et al. (2000). This type of instability corresponds to the limit of strong rotation and weak to moderate source strength. Plume migration along topography was found to produce regular velocity fluctuations, not unlike the variability described by Dickson and Brown (1994). Furthermore, we showed that offshore transport of dense water is highly dependent on the interaction parameter, μ. While coherent baroclinic vortices were not observed in simulations which employed a linearly sloped bottom, these features did evolve in the presence of curved topography. These baroclinic vortex pairs are composed of a domed anomaly of dense fluid, coupled to a strong cyclone in the ambient water, and travel as a unit along topography. They are qualitatively similar to eddies observed in laboratory studies (Whitehead et al. 1990; Lane-Serff and Baines 1998) and to analytical eddy solutions derived in Poulin and Swaters (1999b). A quantitative comparison and an investigation of eddy–topography interaction are both the subject of current research.

The model we have presented clearly neglects many aspects of overflow dynamics, most notably ageostrophic effects, which are likely to play an important role in

cyclone intensification. Indeed, we wished to determine the extent to which variability of density-driven, bottom-trapped currents can be explained by the reduced set of equations (2.9)–(2.12). We feel that the baroclinic mechanism of plume formation, and to some degree cyclogenesis, is captured by this dynamical limit. Our results should also be of relevance in interpreting the findings of in situ, laboratory and computational studies. Nevertheless, several of our assumptions and approximations deserve further attention. For the source flow simulations, we have assumed no-normal-flow conditions on all horizontal boundaries. This is rather unphysical, given that the Denmark Strait outflow is known to include intermediate and surface waters (Spall and Price 1998). The effect of imposed inflow/outflow conditions, or open boundary conditions, should be investigated. Our numerical simulations also neglect the surface-intensified East Greenland Current. The velocity structure associated with this flow could be introduced into the upper layer in order to determine its effect on the dynamics at depth. Another extension of this study is to employ the actual bathymetry of the Irminger Basin, as well as other overflow regions, in order to assess the significance of topographic curvature in vortex development.

APPENDIX

Role of Nof Velocity in Abyssal Currents

An expression for the geostrophic alongslope speed of a steadily traveling patch of fluid with compact support was derived in a reduced-gravity shallow-water setting by Nof (1983). Figure A1 shows a unit point mass situated on a frictionless incline with slope $s^* = \tan(\alpha)$, acted on by gravity and the Coriolis force. Here we denote the alongslope (perpendicular to the page) component of velocity by u. If there is no cross-slope motion, then the projections of the gravitational and Coriolis forces onto the incline must be equal in magnitude and opposite in direction; that is, $f_0 u \cos(\alpha) = -g \sin(\alpha)$. Solving for u, we obtain

$$u = -\frac{g}{f_0}\tan(\alpha) = -\frac{gs^*}{f_0}, \qquad \text{(A.1)}$$

in analogy with (2.1). In this coordinate system s^* is positive so that $u < 0$ (into the page) for $f_0 > 0$. This balance holds for any individual fluid parcel if we neglect interactions with the surrounding fluid.
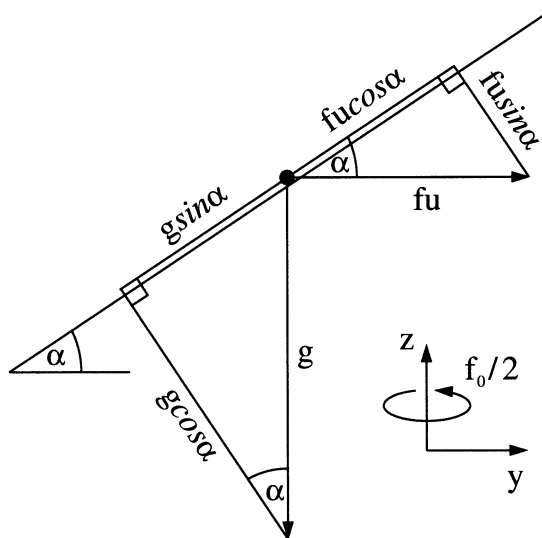

FIG. A1. Simple diagram showing the force balance for a point mass in geostrophic equilibrium, situated on linearly sloping topography. Here the x coordinate points out of the page.

Given a homogeneous current with height $h(y)$, the average geostrophic alongslope speed is simply

$$u_{\text{avg}} = -\frac{g'}{f_0(b-a)} \int_a^b s^* + \frac{dh}{dy}\, dy, \qquad \text{(A.2)}$$

if the cross-slope extent of the current is $a < y < b$. Simplifying,

$$u_{\text{avg}} = -\frac{g'}{f_0}\left[s^* + \frac{h(b)-h(a)}{b-a} \right] \qquad \text{(A.3)}$$

so that whenever $h(a) = h(b)$ the contribution from the current height vanishes, and we are left with the Nof speed. Many geostrophic bottom-dwelling flows are isolated in the cross-slope coordinate such that $h(a) = h(b) = 0$ (Meacham and Stephens 2001). Because the dense plumes south of Denmark Strait also seem to exhibit this property (e.g., Bruce 1995), we feel that the Nof velocity is highly relevant in that case. The above argument may be extended to include bottom friction, which results in a reduced alongslope component of the Nof velocity and a nonzero cross-slope component in the downhill direction. Although in the real ocean interaction with the surrounding fluid can undoubtedly modify these results, we are not aware of any straighforward expression, that can account for this time-dependent dynamics.

REFERENCES

Adams, J., 1989: MUDPACK: Multigrid Fortran Software for the Efficient Solution of Linear Elliptic Partial Differential Equations. *Appl. Math. Comput.,* **34,** 113–146.

Arakawa, A., 1966: Computational design for long term numerical integration of the equations of fluid motion: Two-dimensional incompressible flow. *J. Comput. Phys.,* **1,** 119–143.

Asselin, R. A., 1972: Frequency filter for time integrations. *Mon. Wea. Rev.,* **100,** 487–490.

Bruce, J. G., 1995: Eddies southwest of the Denmark Strait. *Deep-Sea Res.,* **42,** 13–29.

Cooper, L. H. N., 1955: Deep water movements in the North Atlantic as a link between climatic changes around Iceland and biological productivity of the English Channel and Celtic Sea. *J. Mar. Res.,* **14,** 347–362.

Dickson, R. R., and J. Brown, 1994: The production of North Atlantic Deep Water: Sources, rates, and pathways. *J. Geophys. Res.,* **99,** 12 319–12 341.

Etling, D., F. Gelhardt, U. Schrader, F. Brennecke, G. Kuhn, G. C. d'Hieres, and H. Didelle, 2000: Experiments with density currents on a sloping bottom in a rotating fluid. *Dyn. Atmos. Oceans,* **31,** 139–164.

Gawarkiewicz, G., 2000: Effects of ambient stratification and shelf-break topography on offshore transport of dense water on continental shelves. *J. Geophys. Res.,* **105,** 3307–3324.

——, and D. C. Chapman, 1995: A numerical study of dense water formation and transport on a shallow, sloping continental shelf. *J. Geophys. Res.,* **100,** 4489–4507.

Griffiths, R. W., P. D. Killworth, and M. E. Stern, 1982: Ageostrophic instability of ocean currents. *J. Fluid Mech.,* **117,** 343–377.

Hall, M. M., M. McCartney, and J. A. Whitehead, 1997: Antarctic Bottom Water Flux in the equatorial western Atlantic. *J. Phys. Oceanogr.,* **27,** 1903–1926.

Jiang, L., and R. W. Garwood Jr., 1995: A numerical study of three-dimensional dense bottom plumes on a Southern Ocean continental shelf. *J. Geophys. Res.,* **100,** 18 471–18 488.

——, and ——, 1996: Three-dimensional simulations of overflows on continental slopes. *J. Phys. Oceanogr.,* **26,** 1214–1233.

Jungclaus, J. H., J. Hauser, and R. H. Käse, 2001: Cyclogenesis in the Denmark Strait overflow plume. *J. Phys. Oceanogr.,* **31,** 3214–3229.

Karsten, R. H., G. E. Swaters, and R. E. Thomson, 1995: Stability characteristics of deep-water replacement in the Strait of Georgia. *J. Phys. Oceanogr.,* **25,** 2391–2403.

Kikuchi, T., M. Wakatsuchi, and M. Ikeda, 1999: A numerical investigation of the transport process of dense shelf water from a continental shelf to a slope. *J. Geophys. Res.,* **104,** 1197–1210.

Killworth, P. D., 1977: Mixing on the Weddell Sea continental slope. *Deep-Sea Res.,* **24,** 427–448.

Krauss, W., and R. Käse, 1998: Eddy formation in the Denmark Strait Overflow. *J. Geophys. Res.,* **103,** 15 525–15 538.

Lane-Serff, G. F., and P. G. Baines, 1998: Eddy formation by dense flows on slopes in a rotating fluid. *J. Fluid Mech.,* **363,** 229–252.

——, and ——, 2000: Eddy formation by overflows in stratified water. *J. Phys. Oceanogr.,* **30,** 327–337.

LeBlond, P. H., H. Ma, F. Doherty, and S. Pond, 1991: Deep and intermediate water replacement in the Strait of Georgia. *Atmos.–Ocean,* **29,** 288–312.

Meacham, S. P., and J. C. Stephens, 2001: Instabilities of gravity currents along a slope. *J. Phys. Oceanogr.,* **31,** 30–53.

Mellor, G. L., 1996: *Introduction to Physical Oceanography.* AIP Press, 260 pp.

Nof, D., 1983: The translation of isolated cold eddies on a sloping bottom. *Deep-Sea Res.,* **30,** 171–182.

Paldor, N., and P. D. Killworth, 1987: Instabilities of a two-layer coupled front. *Deep-Sea Res.,* **34,** 1525–1539.

——, and M. Ghil, 1990: Finite-wavelength instabilities of a coupled density front. *J. Phys. Oceanogr.,* **20,** 114–123.

Pedlosky, J., 1987: *Geophysical Fluid Dynamics.* 2d ed. Springer-Verlag, 710 pp.

Poulin, F. J., and G. E. Swaters, 1999a: Sub-inertial dynamics of density-driven flows in a continuously stratified fluid on a sloping bottom. I: Model derivation and stability characteristics. *Proc. Roy. Soc. London,* **455A,** 2281–2304.

——, and ——, 1999b: Sub-inertial dynamics of density-driven flows in a continuously stratified fluid on a sloping bottom. II: Isolated eddies and radiating cold domes. *Proc. Roy. Soc. London,* **455A,** 2305–2329.

Price, J. F., and M. O. Baringer, 1994: Outflows and deep water production by marginal seas. *Progress in Oceanography,* Vol. 33, Pergamon, 161–200.

Reszka, M. K., and G. E. Swaters, 2001: Dynamics of bottom-trapped currents with application to the Strait of Georgia. *Can. Appl. Math. Quart.,* in press.

Samelson, R. M., 1998: Large-scale circulation with locally enhanced vertical mixing. *J. Phys. Oceanogr.,* **28,** 712–726.

Shi, X. B., L. P. Røed, and B. Hackett, 2001: Variability of the Denmark Strait Overflow: A numerical study. *J. Geophys. Res.,* **106,** 22 277–22 294.

Smith, P. C., 1975: A streamtube model for bottom boundary currents in the ocean. *Deep-Sea Res.,* **22,** 853–873.

Spall, M. A., and J. F. Price, 1998: Mesoscale variability in Denmark Strait: The PV outflow hypothesis. *J. Phys. Oceanogr.,* **28,** 1598–1623.

Stacey, M. W., S. Pond, and P. H. LeBlond, 1991: Flow dynamics in the Strait of Georgia, British Columbia. *Atmos.–Ocean,* **29,** 1–13.

Sutherland, B. R., and W. R. Peltier, 1994: Turbulence transition and internal wave generation in density stratified jets. *Phys. Fluids,* **6,** 1267–1284.

Swaters, G. E., 1991: On the baroclinic instability of cold-core coupled density fronts on a sloping continental shelf. *J. Fluid Mech.,* **224,** 361–382.

——, 1998: Numerical simulations of the baroclinic dynamics of density-driven coupled fronts and eddies on a sloping bottom. *J. Geophys. Res.,* **103,** 2945–2961.

Tanaka, K., and K. Akitomo, 2001: Baroclinic instability of density current along a sloping bottom and the associated transport process. *J. Geophys. Res.,* **106,** 2621–2638.

Tisseur, F., and K. Meerbergen, 2001: The quadratic eigenvalue problem. *SIAM Rev.,* **43,** 235–286.

Trenberth, K. E., and J. M. Caron, 2001: Estimates of meridional atmosphere and ocean heat transports. *J. Climate,* **14,** 3433–3443.

Whitehead, J. A., M. E. Stern, G. R. Flierl, and B. A. Klinger, 1990: Experimental observations of baroclinic eddies on a sloping bottom. *J. Geophys. Res.,* **95,** 9585–9610.

Wilkinson, J. H., 1965: *The Algebraic Eigenvalue Problem.* Clarendon Press, 662 pp.

Wunsch, C., 1984: The ocean circulation in climate. *The Global Climate,* J. T. Houghton, Ed., Cambridge University Press, 189–203.